International Journal of Heat and Mass Transfer 178 (2021) 121641

Contents lists available at ScienceDirect

International Journal of Heat and Mass Transfer

journal homepage: www.elsevier.com/locate/hmt

Heat transfer and pressure drop of supercritical CO_2 in brazed plate heat exchangers of the tri-partite gas cooler

Alireza Zendehboudi[a,†,*], Zuliang Ye[a,b,†,*], Armin Hafner[a], Trond Andresen[c], Geir Skaugen[c]

[a] Department of Energy and Process Engineering, Norwegian University of Science and Technology (NTNU), Kolbjørn Hejes v 1B, 7491 Trondheim, Norway
[b] School of Energy and Power Engineering, Xi'an Jiaotong University, 28 Xianning West Road, 710049 Xi'an, China
[c] SINTEF Energy Research, Sem Sælands vei 11, 7034 Trondheim, Norway

ARTICLE INFO

Article history:
Received 12 March 2021
Revised 22 June 2021
Accepted 23 June 2021
Available online 10 July 2021

Keywords:
Supercritical carbon dioxide
Brazed plate heat exchanger
Tri-partite gas cooler
Heat transfer
Pressure drop
Correlation

ABSTRACT

The heat transfer characteristic of supercritical CO_2 is an essential research topic due to its significant influence on the performance of heat exchangers and systems. In this paper, the heat transfer and pressure drop of supercritical CO_2 in the brazed plate heat exchangers are experimentally researched. The heat exchangers belong to a tri-partite gas cooler which can simultaneously fulfill the demands of domestic hot water and space heating. The results demonstrates that the thermal resistance in the CO_2 side is the main factor that influences the total heat transfer. The increase of CO_2 inlet pressure can reduce the heat transfer coefficients except at the high temperature region. The improvement of heat transfer coefficient by increasing the CO_2 mass flow rate is more significant in the space heating (SH) and domestic hot water (DHW) preheating gas coolers, and is lowest in the DHW reheating gas cooler. The influence of DHW inlet temperature is more obvious in the DHW preheating gas cooler that connected to the water inlet. The influence of water mass flow rate is different in the DHW and SH operation modes. Moreover, the effects of CO_2 pressure and mass flow rate on the buoyancy force are discussed and the influence of buoyancy force on heat transfer is verified. The inaccuracy of the correlations from the literature is proved and then new correlations are established. The mean absolute relative errors of the new correlations are 11.61% and 12.82% for the one-pass and two-pass configurations, respectively. Furthermore, the frictional pressure drop in the heat exchangers is low (up to 36.51 kPa) and basically increases as the Reynolds number increases.

1. Introduction

According to the Kyoto Protocol, the HFC refrigerants that are extensively used have to be replaced due to their negative impact on the greenhouse effect [1]. Natural refrigerants are considered to be the complete solution for the refrigerant replacement predicament [2]. CO_2 is an excellent candidate due to its non-toxicity, incombustibility, safety, low cost and environmentally benign (ODP = 0, GWP = 1) [3]. It is widely implemented in refrigeration and heat pump systems, air conditioning and various industrial uses [4,5]. Given that one characteristic of CO_2 is the low critical pressure and temperature, the transcritical cycle is introduced to solve the inefficiency problem of the subcritical cycle near the critical point [6]. In the transcritical CO_2 cycle, the heat absorption process occurs at the subcritical pressure whereas the heat rejection process happens at the supercritical pressure [5]. For the water heating application that requires a large temperature lift, the transcritical CO_2 cycle shows a special advantage compared with the traditional refrigerants [7]. The temperature glide of supercritical CO_2 can reduce the heat transfer temperature difference, and decrease the energy loss and entropy generation [8,9].

To demonstrate the merits of transcritical CO_2 heat pump water heater, Saikawa and Koyama [10] studied the coefficient of performance (COP) upper limit of heat pump water heater systems with different refrigerants and the CO_2 system obtained the highest value. The performance of a commercial CO_2 system was compared with that of a similar R134a system by Nawaz et al. [11], and it was discovered that the CO_2 heat pump water heater showed comparable efficiency. Regarding the further exploitation of the performance potential of the transcritical CO_2 heat pump water heater, the design of separated gas coolers for domestic hot water

* Corresponding authors.
E-mail addresses: alireza.zendehboudi@ntnu.no (A. Zendehboudi), zuliangye@foxmail.com (Z. Ye).
† Equal contribution as joint first authors (listed alphabetically).

https://doi.org/10.1016/j.ijheatmasstransfer.2021.121641

Nomenclature

Symbols

A	Heat transfer area [m^2]
b	Corrugation depth of plate [m]
c_p	Isobaric specific heat [J•(kg•K)$^{-1}$]
$\bar{c}_p$	Average isobaric specific heat [J•(kg•K)$^{-1}$]
D	Hydraulic diameter [m]
G	Mass flux [kg•(m^2•s)$^{-1}$]
Gr	Grashof number [-]
g	Gravitational acceleration [m•s^{-2}]
h	Heat transfer coefficient [W•(m^2•K)$^{-1}$]
i	Enthalpy [J•kg^{-1}]
k	Thermal conductivity [W•(m•K)$^{-1}$]
L	Port-to-port length of plate [m]
m	Mass flow rate [kg•s^{-1}]
N	Number [-]
Nu	Nusselt number [-]
P	Pressure [MPa]
p	Corrugation pitch of plate [m]
Pr	Prandtl number [-]
$\overline{Pr}$	Average Prandtl number [-]
Q	Heat transfer rate [W]
Re	Reynolds number [-]
T	Temperature [°C]
t	Thickness of plate [m]
u	Flow velocity [m•s^{-1}]
V	Volumetric flow rate [m^3•s^{-1}]
W	Width of plate [m]
β	Chevron angle of plate [°]
Δp	Pressure drop [kPa]
ΔT	Logarithmic mean temperature difference [K]
μ	Dynamic viscosity [Pa•s]
ρ	Density [kg•m^{-3}]
$\bar{\rho}$	Average density [kg•m^{-3}]
ϕ	Area enlargement factor [-]

Abbreviations

COP	Coefficient of performance
DHW	Domestic hot water
GC	Gas cooler
HT	Heat transfer
GWP	Global warming potential
ODP	Ozone depletion potential
PD	Pressure drop
SH	Space heating

Subscripts

ave	Average
b	Bulk
ch	Channel
CO2	CO_2
f	Frictional
g	Gravitational
in	Inlet
m	Mean
meas	Measured
mp	Manifolds and ports
out	Outlet
p	Plate
port	Port
tot	Total
w	Wall
water	Water

(DHW) production and space heating (SH) has attracted attention due to the superior combination with the supercritical exothermic process [12]. Nekså [13] firstly proposed the system design with two gas coolers that separately fulfill the heating demand of DHW and SH, and the CO_2 from the discharge of compressor initially flows into the DHW gas cooler. Subsequently, the tri-partite gas cooler design was put forward by Stene [14] and could match the temperature profiles of water and CO_2 and improve the energy efficiency of cycle. According to the flow sequence of CO_2 from compressor discharge, the three tube-in-tube heat exchangers were deployed for DHW reheating, SH, and DHW preheating. Furthermore, with the tri-partite gas cooler, the CO_2 system can be very efficient when the SH demand is small compared to the DHW heating demand [15,16].

In the previous publications about the combination of DHW and SH, the heat exchanger type of gas cooler is generally tube-in-tube. Compared to the tube-in-tube type, the brazed plate heat exchanger can provide higher heat transfer performance because of the sinusoidal corrugated pattern, which generates an irregular flow field coupled with intense turbulence and continuous disruption of boundary layers [17]. Moreover, the brazed plate heat exchanger has a compact size, operability at higher pressure, and lower cost than most other compact heat exchangers [18]. Many studies have been carried out on the heat transfer and pressure drop characteristics in brazed plate heat exchangers, and the summary review is shown in Table 1. The studied objects HT and PD denote the heat transfer and pressure drop, respectively. It can be seen that the single-phase, two-phase boiling, two-phase condensation and supercritical fluid in the brazed plate heat exchanger have been investigated. However, the information about supercritical CO_2 has not been published yet. In addition, the existing publications on supercritical CO_2 are mostly conducted based on the research of flowing in channel or tube [5,19,20]. The buoyancy force is an influential factor that affects the heat transfer performance and pressure drop, depending on the operating conditions and flow orientation [5]. For the flowing in circular tubes, the effect of buoyancy on the heat transfer of supercritical fluids was extensively studied by Liao and Zhao [21], Bruch et al. [22], Bae et al. [23], Liu et al. [24], Kim and Kim [25], Zhang et al. [26], and Xu et al. [27]. But most of these publications focused on tubes in the vertical direction, and only Forooghi and Hooman [28] studied the inclined circular tube. Regarding the non-circular geometries, only a few studies have been reported on the heat transfer of supercritical fluids in concentric or eccentric annuli [29,30] and rectangular ducts [31]. Besides, the buoyancy effect in plate heat exchangers has been rarely studied in the literature [32]. Forooghi and Hooman [33] numerically investigated the effect of buoyancy on turbulent convection heat transfer in corrugated channels. They found that if the wall heat flux was kept constant, the Reynolds number must be 3–7 times smaller in corrugated channels compared to a vertical tube so that the buoyancy could influence the heat transfer.

The gas cooler is one of the key components in transcritical CO_2 systems, and the heat transfer and pressure drop of the gas cooler require to be focused [34], which can contribute to the performance improvement of gas cooler and system. The brazed plate heat exchanger is a promising technology for enhancing the efficiency of transcritical CO_2 heat pump. Nonetheless, regarding the application of brazed plate heat exchanger to the tri-partite gas cooler, the relevant study is still in the blank condition. To fill the research gap, the experiments are conducted to analyze the heat transfer and pressure drop of supercritical CO_2 in the brazed plate heat exchangers that constitute the tri-partite gas cooler of a transcritical CO_2 heat pump water heater. The purpose of this paper is to provide a reference for similar applications and to propose the heat transfer correlation that can be easily used.

Table 1
Literature review of the studies on brazed plate heat exchanger.

Author	Year	Method	Fluid	Flow type	Studied object	Correlation
Focke et al. [35]	1985	Experimental	Water	Single-phase	HT & PD	Frictional factor & colburn j-factor
Martin [36]	1996	Theoretical	Water	Single-phase	HT & PD	Frictional factor & Nusselt number
Longo [37]	2008	Experimental	R134a	Two-phase condensation	HT & PD	Frictional pressure drop
Khan et al. [38]	2010	Experimental	Water	Single-phase	HT	Nusselt number
Huang et al. [39]	2012	Experimental	R134a, R507A, R717, R12	Two-phase boiling	HT & PD	Frictional factor & Nusselt number
Forooghi and Hooman [40]	2014	Experimental	98%-pure Perfluoro-butane	Supercritical fluid	HT	Nusselt number
Huang et al. [41]	2015	Experimental	Al_2O_3/water & MWCNT/water nanofluids	Single-phase	HT & PD	Frictional factor & Nusselt number
Longo et al. [42]	2015	Experimental	R236a, R134a, R410A, R600a, R290a, R1270, R1234yf	Two-phase boiling	HT	Heat transfer coefficient
Nilpueng and Wongwises [43]	2015	Experimental	Water	Single-phase	HT & PD	Frictional factor & Nusselt number
Sarraf et al. [44]	2015	Simulation	Water	Single-phase	HT, PD & Flow structure	Frictional factor & Nusselt number
Amalfi and Thome [45,46]	2016	Experimental	R245fa, R236fa	Single-phase	HT & PD	Frictional factor & Nusselt number
Amalfi et al. [17]	2016	Experimental	R245fa	Two-phase boiling	HT & PD	Frictional factor
Barzegarian et al. [18]	2016	Experimental	TiO_2/water nanofluid	Single-phase	HT & PD	Not available
Longo et al. [47]	2016	Experimental	R1234ze(E)	Two-phase boiling	HT & PD	Frictional pressure drop
Desideri et al. [48]	2017	Experimental	R245fa, R1233zd	Two-phase boiling	HT & PD	Frictional pressure drop & heat transfer coefficient
Imran et al. [49]	2017	Experimental	R245fa	Two-phase boiling	HT & PD	Frictional factor & Nusselt number
Nilpueng et al. [50]	2018	Experimental	Water	Single-phase	HT & PD	Frictional factor & Nusselt number
Pourhoseini et al. [51]	2018	Experimental	Silver/water nanofluid	Single-phase	HT	Not available
Shon et al. [52]	2018	Experimental	R1233zd(E)	Two-phase condensation	HT & PD	Frictional factor & Nusselt number
Miyata et al. [53]	2018	Experimental	R134a R1234ze(E)	Supercritical fluid	HT	Not available
Longo et al. [54]	2019	Experimental	R1234ze(Z), R1233zd(E)	Two-phase boiling	HT & PD	Not available
Lee et al. [55]	2020	Experimental	R1234ze(E)	Supercritical fluid	HT & PD	Frictional factor & Nusselt number
Fazeli et al. [56]	2021	Experimental	Water, MWCNT-CuO hybrid nanofluid	Single-phase	HT & PD	Heat transfer coefficient

2. Experimental setup

2.1. System description

To investigate the heat transfer performance in the tri-partite gas cooler, a transcritical CO_2 heat pump water heater system is established. The schematic diagram of the system is shown in Fig. 1. The system consists of the refrigerant circuit, DHW circuit, and SH water circuit. The refrigerant circuit includes a compressor, a tri-partite gas cooler, a high-pressure valve, an evaporator and an internal heat exchanger. The compressor is a reciprocating type, which has a rated displacement of 9.48 $m^3 \bullet h^{-1}$. The tri-partite gas cooler is made of three brazed plate heat exchangers that will be introduced in the latter paragraph. The high-pressure valve can control the gas cooler pressure, and the evaporation temperature can be controlled by the brine inlet temperature of the evaporator to further control the gas cooler inlet temperature.

The DHW and SH water circuits have water pumps and several valves. The valves 2 and 4 can control the return water flow rates at the DHW and SH outlets and manipulate the water inlet temperatures (*T5* for DHW and *T8* for SH). The valves 1 and 2 can control the DHW flow rate, and the valves 3 and 4 can regulate the SH water flow rate. The system can operate under three modes: DHW operation, SH operation and DHW+SH operation. The designing heating capacities of the DHW, SH and DHW+SH operation modes are respectively 10 kW, 8 kW and 10 kW, which can provide the DHW outlet temperature of 70 °C and the SH water outlet temperature of 35 °C. The DHW pump is turned on and the SH pump is stopped under the DHW operation mode, while the status of the pumps is opposite under the SH operation mode. Under the DHW+SH operation mode, both water pumps are turned on.

Table 2
Geometrical characteristics of the three brazed plate heat exchangers.

Parameter	Value
Port-to-port length L (mm)	154.0
Width W (mm)	76.0
Chevron angle β (°)	60
Corrugation depth b (mm)	1.38
Corrugation pitch p (mm)	2.7
Thickness t (mm)	0.23
Area enlargement factor ϕ	1.49
Total number of plates N_p	GC1: 34 GC2: 50 GC3: 14
Diameter of inlet/outlet port D_{port} (mm)	14

2.2. Tested brazed plate heat exchangers

The three brazed plate heat exchangers of the tri-partite gas cooler, which are represented as GC1, GC2 and GC3 (DHW reheating gas cooler, SH gas cooler and DHW preheating gas cooler), are developed by ALFA LAVAL. The used AXP14 model heat exchange plate has a dimension of 190 mm length by 76 mm width. The detailed characteristics of the brazed plate heat exchangers are shown in Fig. 2 and Table 2. The GCs have different functions: for the DHW heating demand, the inlet tap water is firstly preheated by the GC3, and then the intermediate temperature water flows

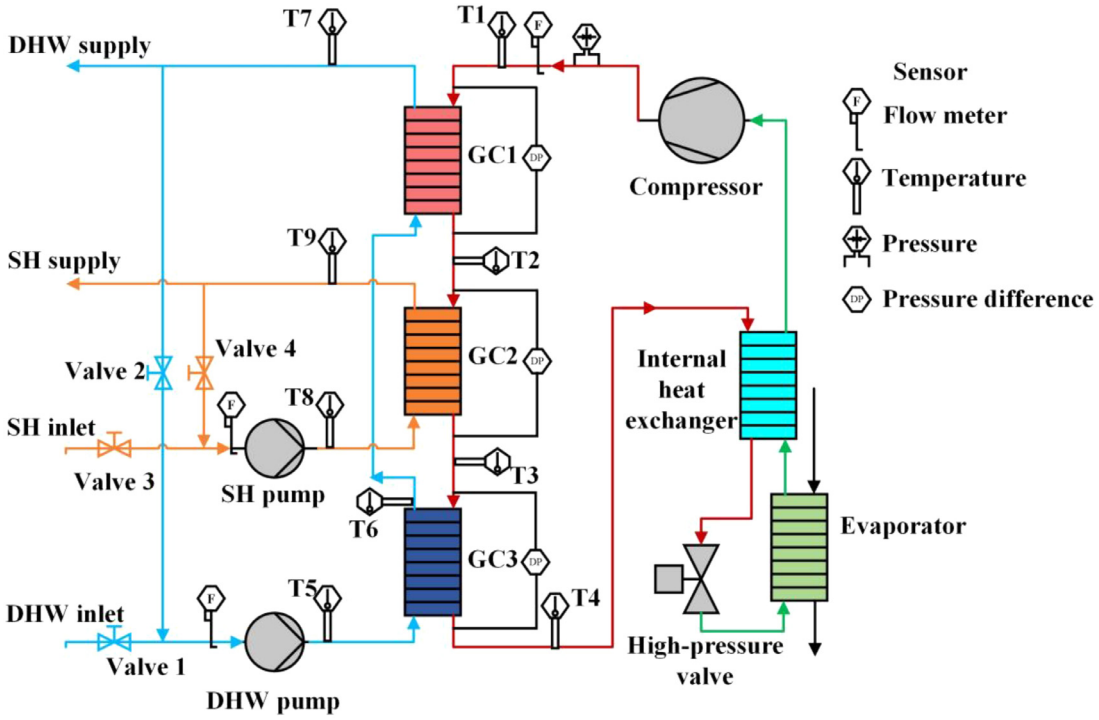

Fig. 1. Schematic diagram of the studied transcritical CO_2 heat pump system.

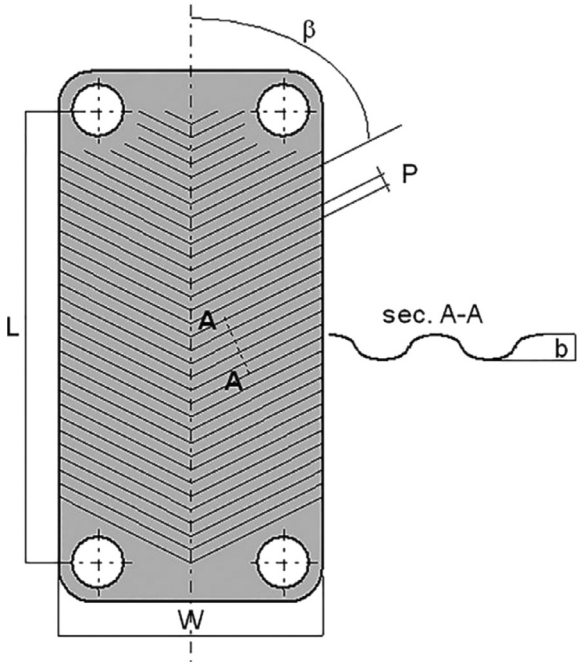

Fig. 2. The schematic of the heat exchange plate [54].

into the GC1 and is reheated to the required high temperature; while the GC2 is used for the SH demand which has a moderate temperature level. The supercritical and high-temperature CO_2 from the compressor successively flows through the GC1, GC2 and GC3, and exchanges heat with water in the counter-flow configuration.

It is worth mentioning that the brazed plate heat exchangers used in this research have two types of internal configuration: one-pass and two-pass, which is shown in Fig. 3. For the one-pass, it means that the water and CO_2 flow between the inlet and outlet distribution ports without changing the flow direction, and thus the water and CO_2 respectively flow upward and downward. While for the two-pass, the fluids in the heat exchanger deflect once, and both the water and CO_2 flow first downward and then upward. In the experiments, the GC2 is always one-pass, and the GC1 and GC3 are tested both with one-pass and two-pass configurations. The tests based on the control variable method are conducted with the one-pass GC2 and two-pass GC1 and GC3. Besides, the experiments with the one-pass GC1 and GC3 are also carried out but the data is only used for analyzing the buoyancy force and the pressure drop, and ultimately fitting the heat transfer correlations.

2.3. Measuring devices

As for the measuring devices, the locations of the applied temperature, pressure and flow rate sensors are displayed in Fig. 1. The Danfoss data recording software (Minilog) is applied to collect and process the output from the sensors. The test facility unit is a comprehensive test rig with many possibilities of experimental investigations involving testing a large range of system configurations and conditions. At the beginning of each experiment, the Danfoss data recording software is switched on, and then the water regulating valves are opened. The water circulation pumps and compressor are turned on. All the controllable process parameters are set to the desired values in the Minilog. The water inlet temperature and mass flow rates of CO_2 and water are adjusted manually by regulating the valves to set the heat transfer between water and CO_2. During the experiments, the parameters logged into the Minilog are continually controlled by following the profiles plotted in the 'Measurement/Graph' tag.

Once the desired values are reached and after steady-state conditions of all parameters are achieved for more than 20 min, the values are recorded as a set of steady data. The time-averaged values of the steady-state are used for this investigation. The characteristics of the measuring devices are shown in Table 3.

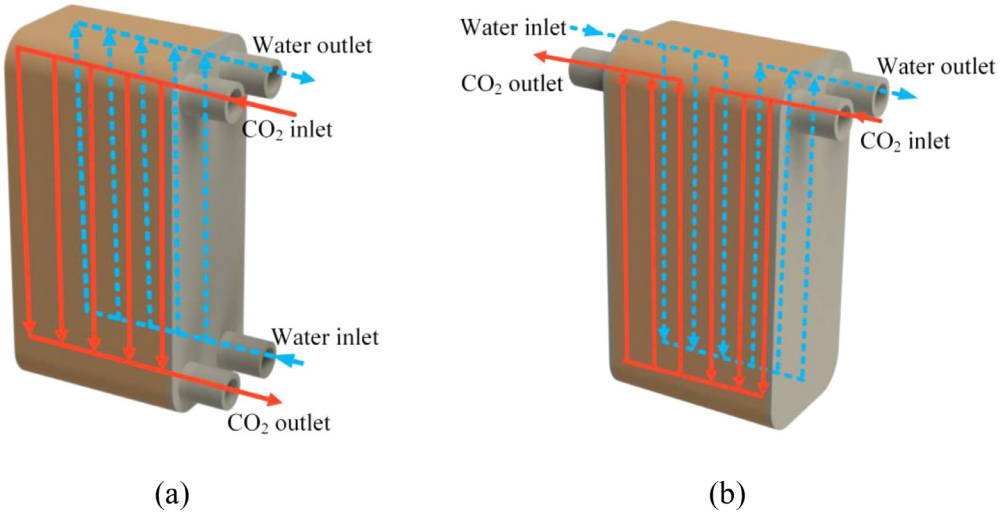

Fig. 3. The (a) one-pass and (b) two-pass internal configurations of the brazed plate heat exchangers.

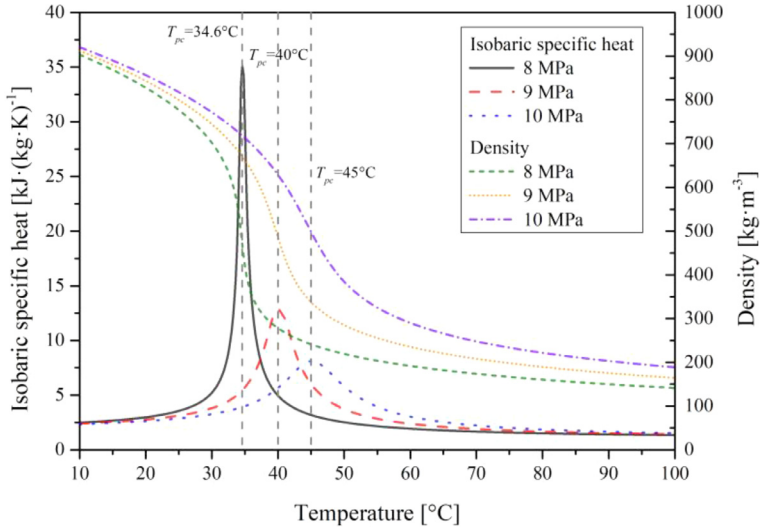

Fig. 4. Variation of isobaric specific heat and density of supercritical CO_2 with the change of temperature under different pressures.

Table 3
Characteristics of the measuring devices.

Parameter	Device	Accuracy
CO_2 pressure	Cerabar PMP71 digital pressure transmitter	±0.25% of span
Pressure difference	Deltabar PMD75 differential pressure transmitter	±0.25% of span
Temperature	PT 1000	±0.15 °C
DHW flow rate	FLR 1000	±3% of span
CO_2 and SH water flow rates	Rheonik RHM 08 Coriolis flow meter	±0.1% of reading

3. Data reduction

In the brazed heat exchangers, the heat transfer rate in the CO_2 side (Q_{CO2}) can be expressed as:

$$Q_{CO2} = m_{CO2}(i_{CO2,in} - i_{CO2,out}) \quad (1)$$

Where m_{CO2} is the CO_2 mass flow rate; $i_{CO2,in}$ and $i_{CO2,out}$ are the CO_2 enthalpy at the inlet and outlet of the heat exchangers. The heat transfer rate in the water side (Q_{water}) can be defined as:

$$Q_{water} = m_{water} c_{p,water}(T_{water,out} - T_{water,in}) \quad (2)$$

Where m_{water} is the water mass flow rate; $c_{p,water}$ is the specific heat of water; $T_{water,out}$ and $T_{water,in}$ are the water outlet and inlet temperatures of the heat exchangers. According to the heat balance, Q_{CO2} and Q_{water} are theoretically supposed to be equal. In the present research, the deviations between these two heat transfer rates are less than 5%. The properties of water and CO_2 are determined by using REFPROP.

The total heat transfer coefficient (h_{tot}) is calculated based on the averaged heat transfer rate (Q_{ave}), the heat transfer area (A) and the actual mean temperature difference (ΔT):

$$h_{tot} = \frac{Q_{ave}}{A\Delta T} \quad (3)$$

where the averaged heat transfer rate can be expressed as:

$$Q_{ave} = \frac{Q_{CO2} + Q_{water}}{2} \quad (4)$$

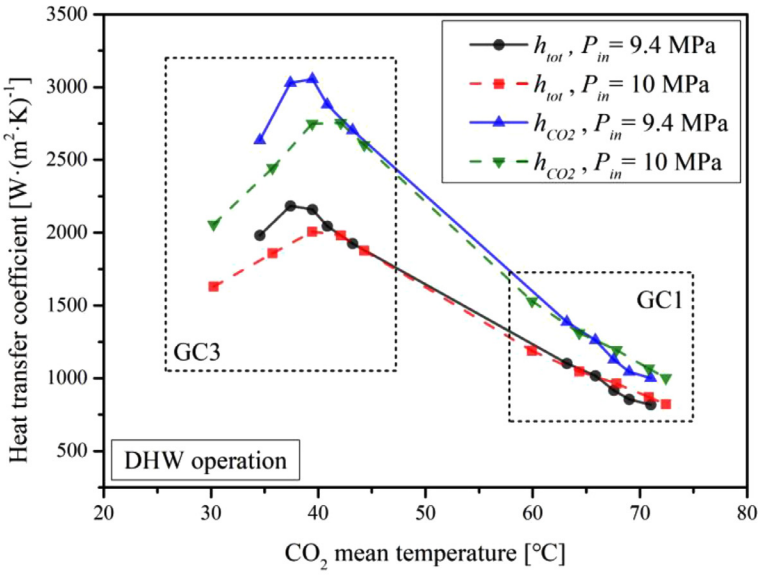

(a)

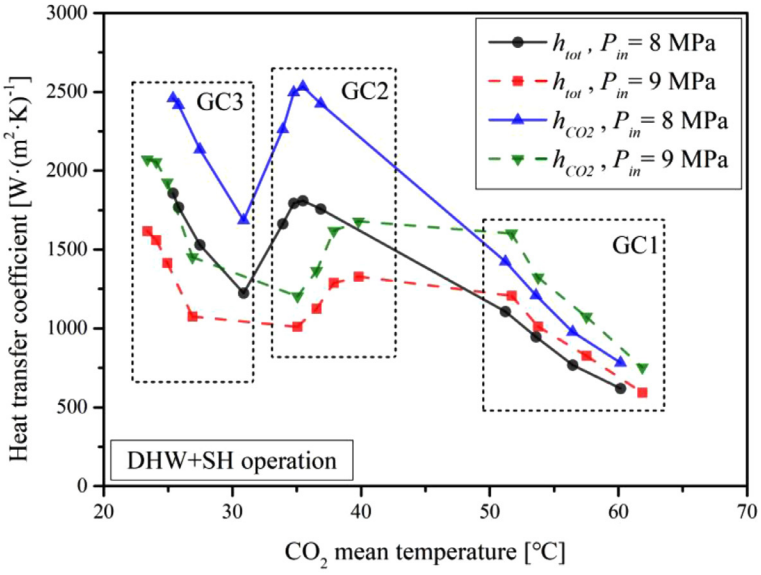

(b)

Fig. 5. Total and CO_2 heat transfer coefficients versus CO_2 mean temperature under different pressures.

The commonly used logarithmic mean temperature difference (LMTD) assumes that both fluids have constant specific heat during the heat transfer process. As shown in Fig. 4, the physical properties of supercritical CO_2 vary significantly with the temperature around its pseudo-critical point. For example, the specific heat of CO_2 reaches a maximum value near pseudo-critical temperature for all considered pressures. The peak value of specific heat decreases as the pressure increases and the variations of the specific heat with temperature becomes relatively flat at the temperatures away from the pseudo-critical point. The density shows sharp downward trend with an increase in temperature. At one particular temperature, small temperature variation causes a sharp drop in the values, and the curves become nearly vertical for the lower pressures. Therefore, the LMTD method is not valid for the experimental conditions conducted in this study.

To obtain the actual mean temperature difference in Eq. (3), the *UA* is calculated based on its definition :

$$UA = \int_0^{A_{tot}} U dA = \int_0^{Q_{tot}} \frac{dQ}{\Delta T} \tag{5}$$

To obtain the numerically integrated result of Eq. (5), the heat transfer process is equally divided into *N* segments with the same heat transfer rate (δ_Q). In each segment, the temperature difference is obtained based on the energy balance. Therefore, the *UA* can be numerically integrated as:

$$UA = \sum_{i=1}^{N} \frac{\delta Q}{\Delta T_i} \tag{6}$$

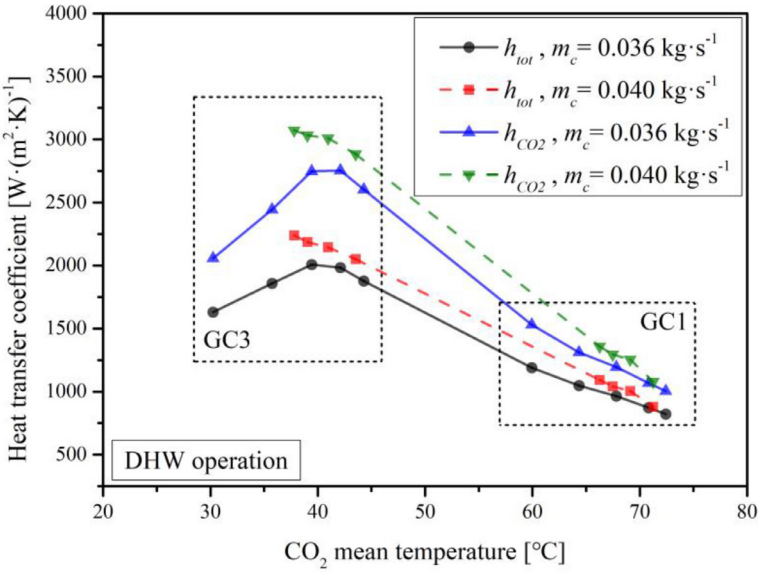

(a)

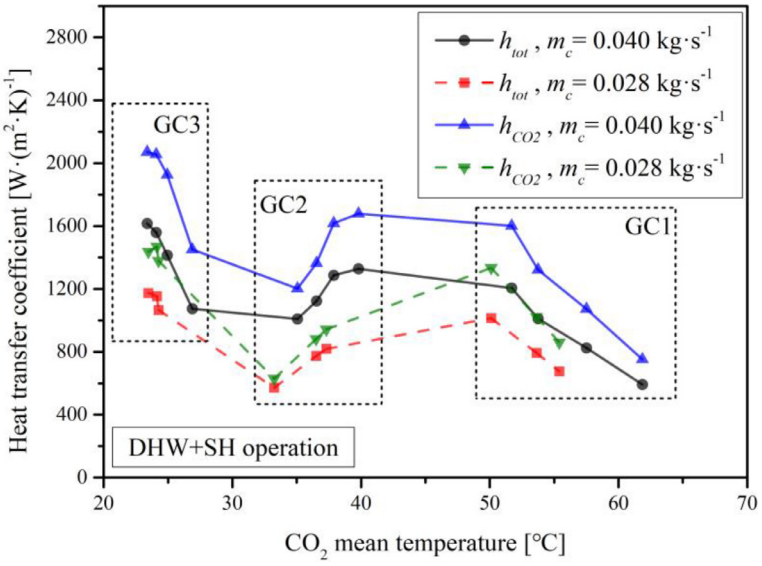

(b)

Fig. 6. Total and CO_2 heat transfer coefficients versus CO_2 mean temperature under different CO_2 mass flow rates.

Using the *UA*, the actual mean temperature difference (ΔT) can be determined:

$$\Delta T = \frac{Q_{tot}}{UA} \tag{7}$$

where Q_{tot} is equal to Q_{ave} in this study.

The heat transfer area (A) of the brazed plate heat exchangers can be calculated as [52]:

$$A = \phi W L N_p \tag{8}$$

where ϕ is the area enlargement factor that considers the increase of area due to the corrugation on the plates; W, L and N_p are the width, port-to-port length and number of the heat exchange plates, respectively. The area enlargement factor is defined as:

$$\phi \approx (1 + \sqrt{1+X^2} + 4\sqrt{1+X^2/2})/6 \tag{9}$$

where

$$X = \frac{\pi b}{p} \tag{10}$$

Similarly, due to the change of specific heat, the CO_2 temperature would nonlinearly vary during the heat transfer process. Therefore, to obtain the CO_2 temperature at which the thermodynamic properties are defined, the commonly used concept of bulk temperature that is the average of inlet and outlet temperatures [22,57] cannot fulfill the requirement. Instead, the concept of CO_2 mean temperature (T_m) is adopted:

$$T_m = \frac{\sum_{i=1}^{N} T_{CO2,i}}{N} \tag{11}$$

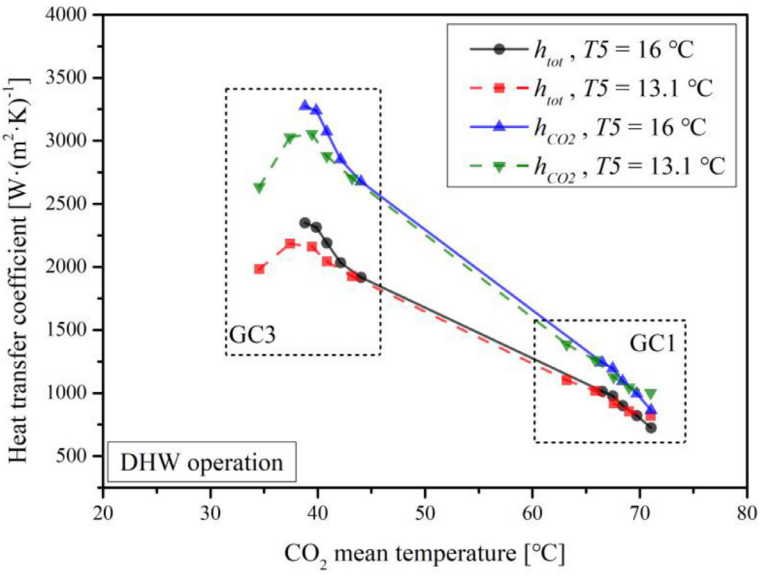

(a)

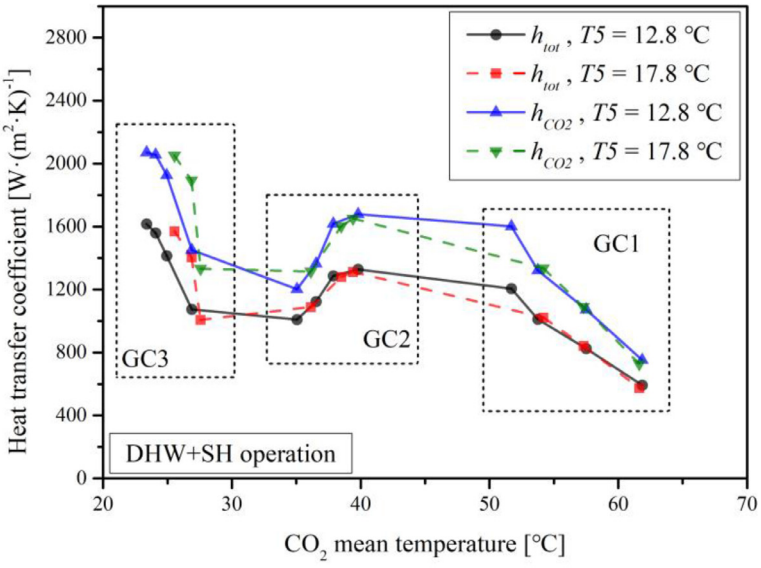

(b)

Fig. 7. Total and CO_2 heat transfer coefficients versus CO_2 mean temperature under different water inlet temperatures.

The total heat transfer coefficient comprises the CO_2 and water side heat transfer coefficients and the wall thermal resistance. It can be also expressed as:

$$\frac{1}{h_{tot}} = \frac{1}{h_{CO2}} + \frac{1}{h_{water}} + \frac{t}{k_w} \tag{12}$$

where h_{CO2} and h_{water} are the heat transfer coefficients in the CO_2 and water sides; t is the thickness of the plate; k_w is the thermal conductivity of the wall. h_{water} is calculated by applying the correlation of Huang et al. [41] because the plate geometry and the range of Reynolds number are similar to those of the studied heat exchangers.

$$Nu_{water} = 0.2302\mathrm{Re}_{water}^{0.745} Pr_{water}^{0.4} \tag{13}$$

$$h_{water} = \frac{Nu_{water} k_{water}}{D} \tag{14}$$

The hydraulic diameter (D) can be defined as:

$$D = \frac{2b}{\phi} \tag{15}$$

where b is the corrugation depth of the plate. The Reynolds number (Re) can be calculated as:

$$\mathrm{Re} = \frac{\rho u D}{\mu} \tag{16}$$

where u is the flow velocity of fluid and is defined as:

$$u = \frac{V}{bWN_{ch}} \tag{17}$$

where ρ and μ are the density and dynamic viscosity of the fluid; V is the volumetric flow rate; N_{ch} is the number of the channels for fluid.

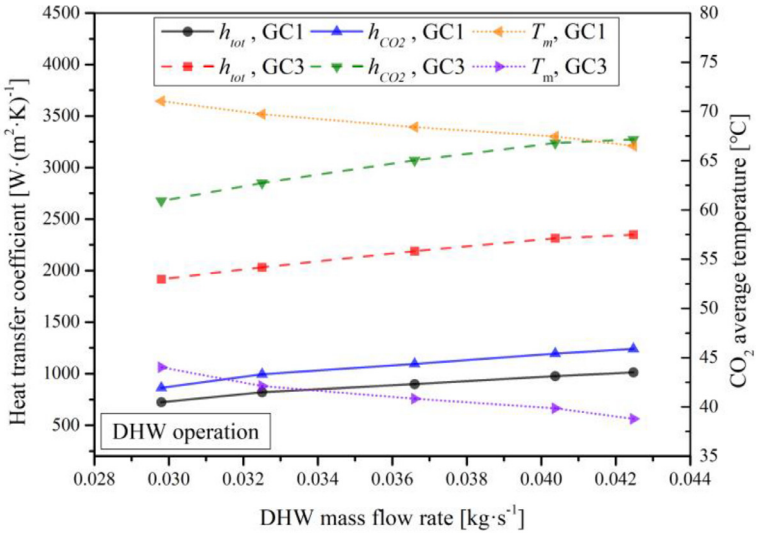

(a)

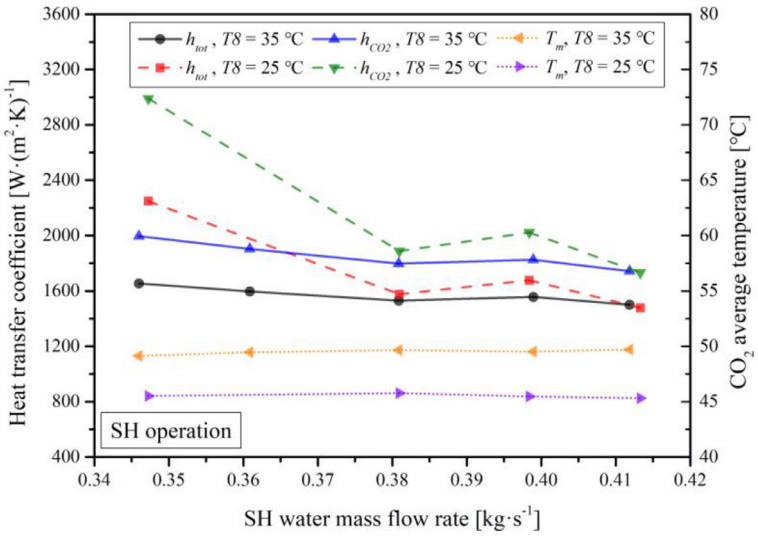

(b)

Fig. 8. Total and CO_2 heat transfer coefficients and CO_2 mean temperature versus water mass flow rates.

The measured pressure drop (Δp_{meas}) of the heat exchangers consists of the frictional pressure drop (Δp_f), the gravitational pressure drop (Δp_g) and the pressure drop of the manifolds and ports (Δp_{mp}) [48,50]. Thus, the frictional pressure drop can be defined as:

$$\Delta p_f = \Delta p_{meas} - \Delta p_g - \Delta p_{mp} \tag{18}$$

The gravitational pressure drop is determined by:

$$\Delta p_g = g\rho_m L \tag{19}$$

where ρ $\underline{m}$ is the density at the CO_2 mean temperature. The pressure drop of the manifolds and ports is defined as:

$$\Delta p_{mp} = 1.5\frac{G_{port}^2}{2\rho_m} \tag{20}$$

where G_{port} is the CO_2 mass flux at the cross section of the port.

Based on the method proposed by Moffat [58], the uncertainty analysis is conducted. The uncertainties of h_{tot}, h_{water}, h_{CO2} and Δp_f are 8.16%, 4.59%, 11.76% and 2.73%, respectively.

4. Results and discussion

4.1. Heat transfer

4.1.1. Effect of CO_2 inlet pressure

Fig. 5 shows the total and CO_2 side heat transfer coefficients (h_{tot} and h_{CO2}) versus the CO_2 mean temperature under the inlet pressure of 9.4 MPa and 10 MPa. The results are obtained under the DHW operation mode at CO_2 inlet temperature of 97 °C, CO_2 mass flow rate of 0.0358 kg•s $^{-1}$, water inlet temperature of 13.1 °C and DHW mass flow rate of 0.030 - 0.043 kg•s $^{-1}$. The dashed rectangles indicate the data groups for each gas cooler that the data points belong to. The data points with different CO_2 mean temperatures are achieved by adjusting the DHW mass flow rate, and the larger the DHW mass flow rate the lower the CO_2 mean temperature.

The averaged h_{tot}, h_{water} and h_{CO2} from all data are 1380.2, 6094.1 and 2035.0 W•(m^2•K)$^{-1}$, which suggests that the thermal resistance at the CO_2 side basically dominates the total heat trans-

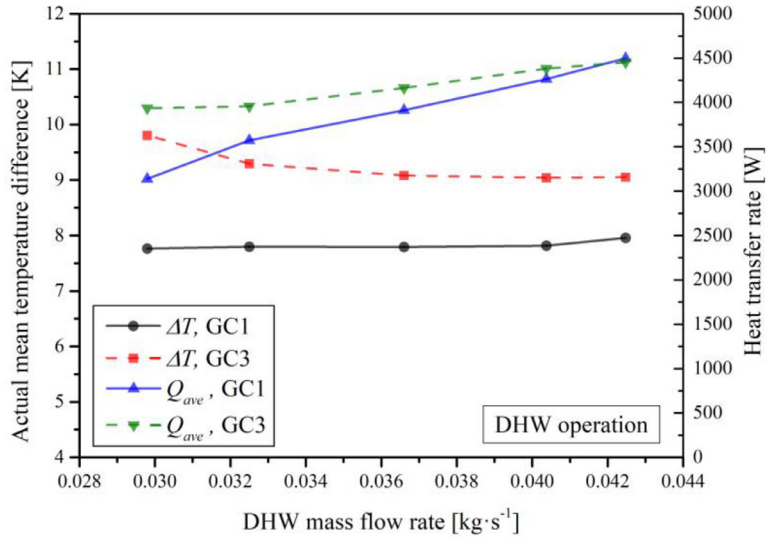

(a)

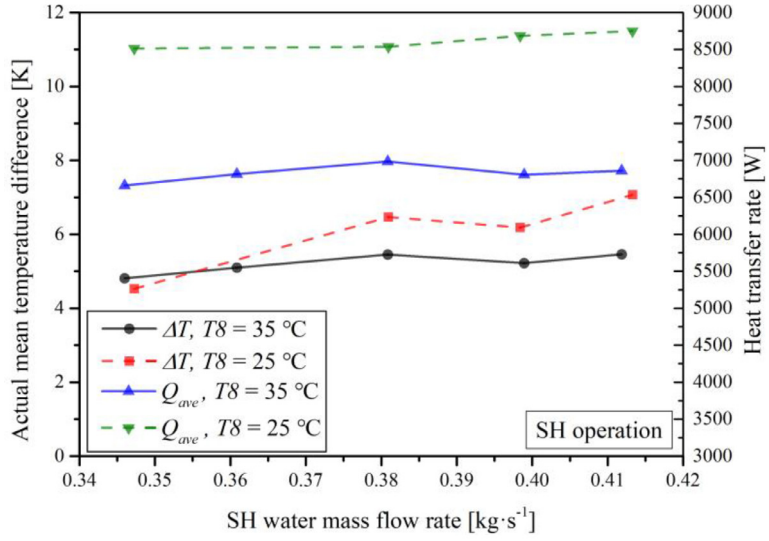

(b)

Fig. 9. Heat transfer rates and actual mean temperature differences versus water mass flow rate corresponding to the results of Fig. 8.

fer. As shown in Fig. 5(a), given the different heating functions of GC1 and GC3, the corresponding CO_2 mean temperatures are divided into two groups. The reheating GC1 has higher CO_2 mean temperatures and low heat transfer coefficients due to the low specific heat in this gas-like supercritical region. Whereas, the preheating GC3 shows an operation near the pseudo-critical temperature (42.04 °C for 9.4 MPa and 45 °C for 10 MPa). The dramatic increase of specific heat in the vicinity of the pseudo-critical point leads to the higher heat transfer coefficients of GC3. Moreover, with the increase of CO_2 mean temperature, the heat transfer coefficients increase and then decrease, and thus peak values appear. For GC3, at the pressure of 9.4 MPa, the peak values of h_{tot} and h_{CO2} are higher than those at the pressure of 10 MPa.

Fig. 5(b) displays the results under the DHW+SH operation mode at CO_2 inlet temperature of 80 °C, CO_2 mass flow rate of 0.040 kg•s $^{-1}$, DHW inlet temperature of 12.8 °C, SH water inlet temperature of 30 °C, SH water mass flow rate of 0.1917 kg•s $^{-1}$ and DHW mass flow rate of 0.0167 - 0.0417 kg•s $^{-1}$. The heat transfer coefficients in the GC1 and GC3 show an increasing trend with the decrease of CO_2 mean temperature. The reason is that the decrease of CO_2 mean temperature is attributed to the increase of DHW mass flow rate, and the associated increasing water flow velocity enhances the water side heat transfer coefficient, which improves the total heat transfer coefficient. Besides, the variation of thermodynamic properties in the liquid-like supercritical region is also small and accordingly has an unimportant impact on GC3 under DHW+SH operation. As for GC2, the CO_2 mean temperatures are close to the pseudo-critical temperature (T_{pc}= 34.63 °C for P = 8 MPa and T_{pc}= 40 °C for P = 9 MPa), and the pressure significantly influences the thermodynamic properties including specific heat and thermal conductivity. For both h_{tot} and h_{CO2} in GC2, the maximum values at 8 MPa are greater than those at 9 MPa. In addition, with the increase of pressure, the temperature corresponding to the maximal heat transfer coefficient in GC2 increases because of rising pseudo-critical temperature.

Table 4
The effects of parameters on the averaged Reynolds number and heat transfer coefficients.

Variable	Item	Condition	DHW operation GC1	GC3	Condition	DHW+SH operation GC1	GC2	GC3
CO_2 pressure (P_{in})	$\overline{Re}_m$	9.4 MPa	3672.9	4979.8	8 MPa	4389.2	941.1	3855.6
		10 MPa	3474.8	4350.9	9 MPa	4007.7	678.2	3320.8
		Variation	−5.4%	−12.6%	Variation	−8.7%	−27.9%	−13.9%
	$h_{tot,ave}$	9.4 MPa	941.4	2058.7	8 MPa	859.6	1755.4	1594.5
		10 MPa	977.8	1870.5	9 MPa	909.1	1187.4	1416.0
		Variation	3.9%	−9.1%	Variation	5.8%	−32.4%	−11.2%
	$h_{CO2,ave}$	9.4 MPa	1163.5	2860.4	8 MPa	1097.5	2429.2	2173.8
		10 MPa	1220.5	2521.1	9 MPa	1187.1	1465.9	1876.2
		Variation	4.9%	−11.9%	Variation	8.2%	−39.7%	−13.7%
CO_2 mass flow rate (m_c)	$\overline{Re}_m$	0.036 kg•s $^{-1}$	3474.8	4350.9	0.028 kg•s $^{-1}$	2758.8	420.4	2277.3
		0.040 kg•s $^{-1}$	3977.2	5343.6	0.040 kg•s $^{-1}$	4007.7	678.2	3320.8
		Variation	14.5%	22.8%	Variation	45.3%	61.3%	45.8%
	$h_{tot,ave}$	0.036 kg•s $^{-1}$	977.8	1870.5	0.028 kg•s $^{-1}$	827.9	721.5	1132.1
		0.040 kg•s $^{-1}$	1003.5	2154.9	0.040 kg•s $^{-1}$	909.1	1187.4	1416.0
		Variation	2.6%	15.2%	Variation	9.8%	64.6%	25.1%
	$h_{CO2,ave}$	0.036 kg•s $^{-1}$	1220.5	2521.1	0.028 kg•s $^{-1}$	1072.6	818.1	1429.0
		0.040 kg•s $^{-1}$	1245.7	2999.2	0.040 kg•s $^{-1}$	1187.1	1465.9	1876.2
		Variation	2.1%	19.0%	Variation	10.7%	79.2%	31.3%
DHW inlet temperature ($T5$)	$\overline{Re}_m$	13.1 °C	3672.9	4979.8	12.8 °C	4007.7	678.2	3320.8
		16 °C	3615.8	5553.3	17.8 °C	4032.2	711.4	3462.5
		Variation	−1.6%	11.5%	Variation	0.6%	4.9%	4.3%
	$h_{tot,ave}$	13.1 °C	941.4	2058.7	12.8 °C	909.1	1187.4	1416.0
		16 °C	886.5	2160.8	17.8 °C	812.9	1227.4	1327.7
		Variation	−5.8%	5.0%	Variation	−10.6%	3.4%	−6.2%
	$h_{CO2,ave}$	13.1 °C	1163.5	2860.4	12.8 °C	1187.1	1465.9	1876.2
		16 °C	1077.4	3022.7	17.8 °C	1051.3	1523.1	1759.2
		Variation	−7.4%	5.7%	Variation	−11.4%	3.9%	−6.2%

The impact of pressure on the heat transfer coefficient is due to the variations of CO_2 thermodynamic properties caused by changing pressure. The variations become more dramatic when the pressure is closer to the critical pressure. As seen from Fig. 5, the variation trend of the heat transfer coefficient is similar to that of specific heat under different operating pressures. The trend demonstrates that the heat transfer coefficients are higher in the liquid-like region for lower pressures, while the values for lower pressure are lower in the gas-like region. The peak value of specific heat increases significantly near the critical point by decreasing operating pressure; therefore, the heat transfer coefficient tends to lift sharply in this region and the heat transfer is the best at the pseudo-critical point.

To show the influence of parameters quantitively, the results are summarized in Table 4. $\overline{Re}_m$, $h_{tot,ave}$ and $h_{CO2,ave}$ are the averages of the CO_2 Reynolds number and the heat transfer coefficients based on the data points in Fig. 5,Fig. 6 and Fig. 7. The comparisons ignore the influence of CO_2 mean temperature and only focus on the numerical values. With the result at the lower value of variables as the reference value, the variations are determined. From Table 4, it can be observed that with the increase of pressure, the averaged heat transfer coefficients decrease except in the GC1, and the reductions reach up to 32.4% and 39.7% for $h_{tot,ave}$ and $h_{CO2,ave}$, respectively.

4.1.2. Effect of CO_2 mass flow rate

Fig. 6(a) shows the results under DHW operation mode with different CO_2 mass flow rates at CO_2 inlet pressure of 10 MPa, CO_2 inlet temperature of 97 °C, DHW inlet temperature of 13.1 °C, and DHW mass flow rate of 0.030 - 0.043 kg•s $^{-1}$. It can be observed that the increase of CO_2 mass flow rate leads to the increase of h_{tot} and h_{CO2}. The higher CO_2 mass flow rate generates the increase of the Reynolds number and the diffusion rate, and then enhances the heat transfer coefficients.

Fig. 6(b) shows the results under DHW+SH operation mode at CO_2 inlet pressure of 9 MPa, CO_2 inlet temperature of 80 °C, DHW inlet temperature of 12.8 °C, SH water inlet temperature of 30 °C, and SH water mass flow rate of 0.1917 kg•s $^{-1}$. Increasing the CO_2 mass flow rate significantly improves the heat transfer coefficients. It can be found from Table 4 that the influence of CO_2 mass flow rate is the largest. In all conditions, the averaged heat transfer coefficients are enhanced with the increase of the CO_2 mass flow rate. Under the DHW and DHW+SH operation modes, the enhancement of heat transfer coefficients in the GC1 is the lowest while the improvement is much more significant in the GC2 and GC3.

4.1.3. Effect of water inlet temperature

Fig. 7(a) depicts the heat transfer coefficients under DHW operation mode with different DHW inlet temperature at CO_2 inlet pressure of 9.4 MPa, CO_2 inlet temperature of 97 °C, and CO_2 mass flow rate of 0.0358 kg•s $^{-1}$. As shown, no significant influence of the water inlet temperature can be found in the results of GC1. However, because the water inlet is directly linked to GC3, the influence is more obvious and the heat transfer coefficients are increased by the increase of DHW inlet temperature.

Fig. 7(b) shows the results under the DHW+SH operation mode at CO_2 inlet pressure of 9 MPa, CO_2 inlet temperature of 80 °C, CO_2 mass flow rate of 0.040 kg•s $^{-1}$, SH water inlet temperature of 30 °C, and SH water mass flow rate of 0.1917 kg•s $^{-1}$. Similarly, the effect of water inlet temperature is larger when the heat exchanger is close to the water inlet. The increase of temperature from 12.8 °C to 17.8 °C results in an ignorable impact on the heat transfer coefficients in the high temperature state. Compared with the CO_2 pressure and mass flow rate, the water inlet temperature has a relatively small effect. From Table 4, the variations caused by increase of DHW water inlet temperature are all lower than 12%.

4.1.4. Effect of water mass flow rate

Fig. 8 shows the effects of DHW and SH water mass flow rates on the heat transfer coefficients, and the variations of CO_2 mean temperatures with the change of water mass flow rates are depicted as well. For the DHW operation in Fig. 8(a), the CO_2 inlet pressure, CO_2 inlet temperature, CO_2 mass flow rate and DHW in-

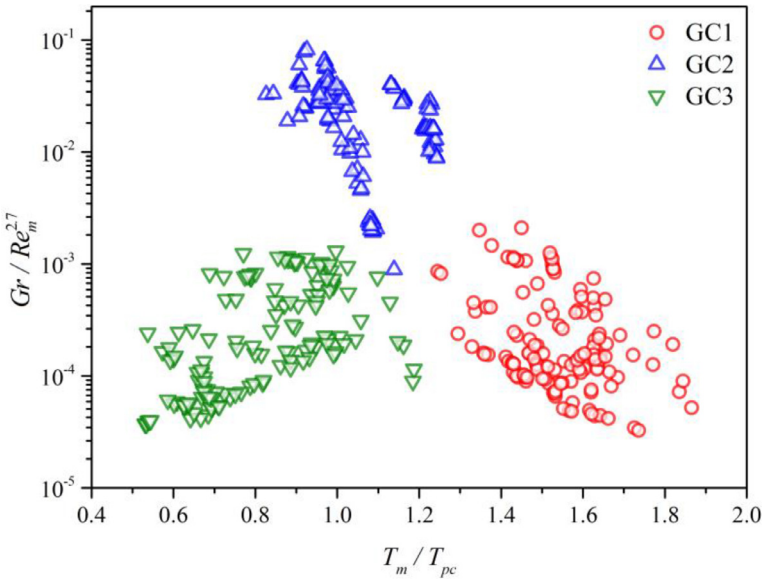

Fig. 10. The buoyancy forces in the three GCs.

let temperature are 9.4 MPa, 97 °C, 0.0358 kg•s $^{-1}$ and 16 °C, respectively. As the DHW mass flow rate increases, the heat transfer coefficients of GC1 and GC3 increase, and the CO_2 mean temperature decreases. The CO_2 mean temperature in GC3 is closer to the pseudo-critical point, which leads to larger heat transfer coefficients. Fig. 8(b) presents the situation under the SH operation mode at CO_2 inlet pressure of 9 MPa, CO_2 inlet temperature of 76 °C and CO_2 mass flow rate of 0.040 kg•s $^{-1}$. The CO_2 mean temperatures are nearly constant with the change of SH water mass flow rate. It can be seen that when the SH water inlet temperature is 25 °C, the heat transfer coefficients are higher than those at 35 °C, which results from the higher specific heat caused by the lower CO_2 mean temperature. Different from the DHW operation mode, the increase of SH water mass flow rate under the SH operation mode conduces to the decreasing trend of heat transfer coefficients. This discrepancy is attributed to the different variations of heat transfer rate and temperature difference under the DHW and SH operation modes.

Fig. 9 displays the results related to the conditions in Fig. 8. As can be seen in Fig. 9(a), the heat transfer rates of GC1 and GC3 rise with the increase of DHW mass flow rate. However, the temperature differences show different trends. The increase of DHW mass flow rate slightly affects ΔT for GC1 but results in the decrease of ΔT for GC3. According to Eq. (3), the total heat transfer coefficients of GC1 and GC3 are enhanced.

Based on Eq. (3), the decreasing trend of heat transfer coefficients under SH operation mode can be explained as well. In Fig. 9(b), with the increase of SH water mass flow rate, the actual mean temperature difference presents the increasing trend, but the increase of ΔT at the SH water inlet temperature of 35 °C is relatively small. In addition, the change of heat transfer rates is marginal. Thus, the reduction of heat transfer coefficients is the consequence of the increase of actual mean temperature difference.

4.1.5. Effect of buoyancy force

According to the literature, the heat transfer performance of the supercritical CO_2 is also significantly affected by the buoyance force in some conditions [59]. Based on the effects of buoyancy force on the flow and heat transfer, the flow of supercritical CO_2 can be divided into forced and mixed convections [60]. The buoyancy force has an important influence on the heat transfer in the mixed convection, while in the forced convection, the influence is negligible. The large density gradient caused by a large radial temperature gradient is an essential condition where the buoyancy force can affect the heat transfer.

For the in-tube flowing, when the following equation is satisfied, the buoyancy force cannot be ignored in the heat transfer of supercritical CO_2 [61]:

$$Gr/\mathrm{Re}^{2.7} > 10^{-5} \tag{21}$$

Where Gr is the Grashof number and can be defined in this paper as:

$$Gr = \frac{(\overline{\rho}_w - \rho_m)\rho_m g D^3}{\mu_m^2} \tag{22}$$

Where g is the acceleration of gravity and $\bar{\rho}_w$ is the density at the averaged wall temperature [62]:

$$\bar{\rho}_w = \frac{\int_{T_w}^{T_m} \rho dT}{T_m - T_w} \tag{23}$$

However, because of the complex geometry in the brazed plate heat exchanger, this criterion cannot be applied. Moreover, the work considering the buoyancy effect in plate heat exchanger is rare [32], and with our best knowledge, there is no publication that suggests the criterion for buoyancy effect in plate heat exchanger.

Fig. 10 shows the buoyancy forces in the three GCs. The largest buoyancy force exists in the GC2, which has the maximum number of the heat exchange plates and accordingly the largest flow area and the lowest CO_2 flow velocity. The GC1 has more plates than GC3 and thus the CO_2 flow velocity could be lower in GC1, which is supposed to result in the higher buoyancy force effect. But the buoyancy forces in GC1 and GC3 are at a similar level. It is because the high temperature and low density in GC1 counteract the influence of plate number on the flow velocity.

To further investigate the buoyancy force, the effects of CO_2 pressure and CO_2 mass flow are shown in Fig. 11. The results in Fig. 11 are obtained under the conditions of Fig. 5 and Fig. 6. As Fig. 11(a) shows, the influence of pressure on the buoyancy force is different according to the temperature. Obviously, the buoyancy force declines with the lower pressure when the CO_2 mean temperature is high in the GC1. On the contrary, when the temperature is relatively low in the GC3, the buoyancy force is slightly improved by the decrease of pressure. In the GC2, both two types

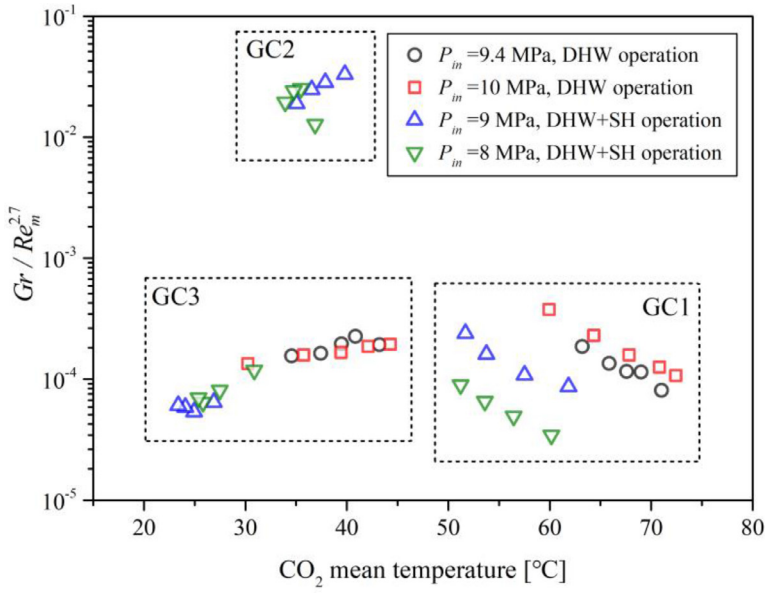

(a)

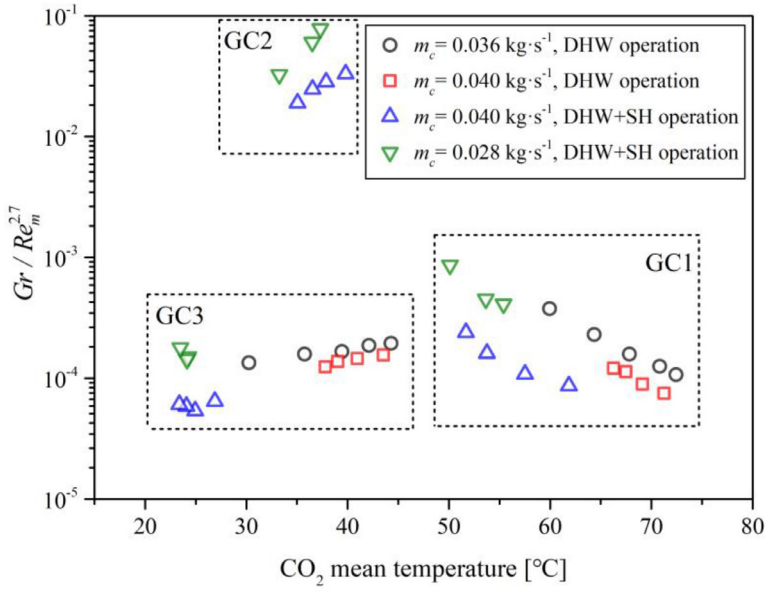

(b)

Fig. 11. The effects of CO_2 inlet pressure and CO_2 mass flow rate on the buoyancy force.

of effects of pressure occur. In comparison, the effect of CO_2 mass flow rate is consistent at all temperatures. The lower the CO_2 mass flow rate the higher the buoyancy force because of the smaller flow velocity and weaker turbulence.

To investigate the effect of buoyancy force on the heat transfer, the Nusselt number versus $Gr/Re^{2.7}$ is shown in Fig. 12. The results in Fig. 12 are also obtained under the conditions of Fig. 5 and Fig. 6. Except the GC3 at 8 MPa under the DHW+SH operation mode, the Nusselt number generally shows an increasing trend with the increase of buoyancy force. Therefore, the buoyancy force has an influence on the heat transfer of supercritical CO_2 in this research, which would be considered in the following correlation development.

4.2. Heat transfer correlation development

In the previous publications, the in-tube heat transfer of supercritical CO_2 during the cooling and heating process has been extensively studied [5]. However, the research on the supercritical heat transfer of CO_2 in the brazed plate heat exchanger has not been reported yet. The heat transfer coefficient of supercritical fluids is difficult to be predicted accurately due to the drastic variation of thermodynamics properties [63]. Moreover, the validity of published correlations is limited by the experimental data, and the availability is reliable only within a certain range.

Fig. 13 shows the comparison of experimental Nusselt numbers and the calculated results based on the correlations from Bruch et al. [22], Liu et al. [57], Forooghi and Hooman [40], Lee et al.

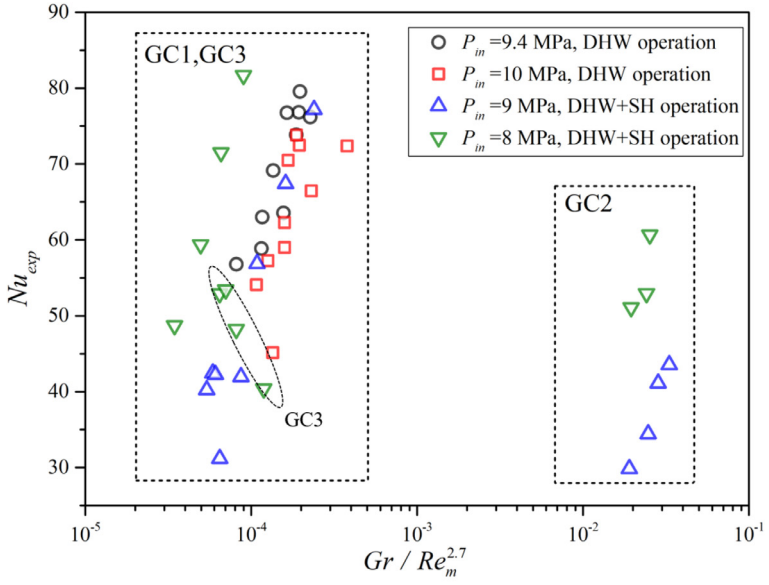

(a)

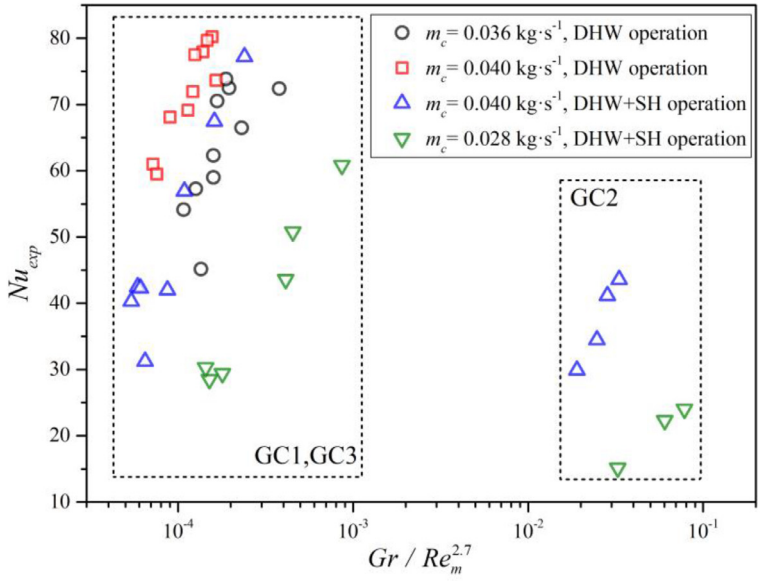

(b)

Fig. 12. The effect of buoyancy force on the Nusselt number.

[55] and Khan et al. [38]. Table 5 shows the five correlations used for comparison and their application conditions. Among these five correlations, two are for supercritical CO_2 in-tube flow, two are for supercritical fluids in plate heat exchanger, and one is for single phase fluid in plate heat exchanger. The application ranges of Reynolds number (or mass flux) of these correlations partially overlap the values in our research.

It can be discovered that the predictions of Bruch et al.'s and Liu et al.'s correlations are basically lower than the experimental values, and there are massive data points where the relative error is lower than −60% or even −90%. It indicates that the correlations established based on the research of in-tube flow are not suitable for the situation in the brazed plate heat exchanger. The complex geometry of plate enhances the heat transfer performance. Many prediction points based on the correlations from Lee et al. and Khan et al. have an error larger than 90%. The mean absolute relative errors of the correlations from Bruch et al., Liu et al., Forooghi and Hooman, Lee et al. and Khan et al. are 71.6%, 67.9%, 41.1%, 495.3% and 138.1%, respectively. The correlation from Forooghi and Hooman shows the best accuracy but is still not satisfactory. Therefore, the specialized correlations are necessary to describe the heat transfer of supercritical CO_2 in the brazed plate heat exchanger.

Considering the influence of thermodynamics properties at the CO_2 mean temperature and the wall temperature and the effect of buoyance force, the correlations are proposed based on the least square method according to the below expression [62]:

$$Nu = a_1 \mathrm{Re}_m^{a_2} \overline{Pr}_m^{a_3} \left(\frac{\rho_w}{\rho_m}\right)^{a_4} \left(\frac{\bar{c}_p}{c_{p,m}}\right)^{a_5} \left(\frac{Gr}{\mathrm{Re}_m^{2.7}}\right)^{a_6} \quad (24)$$

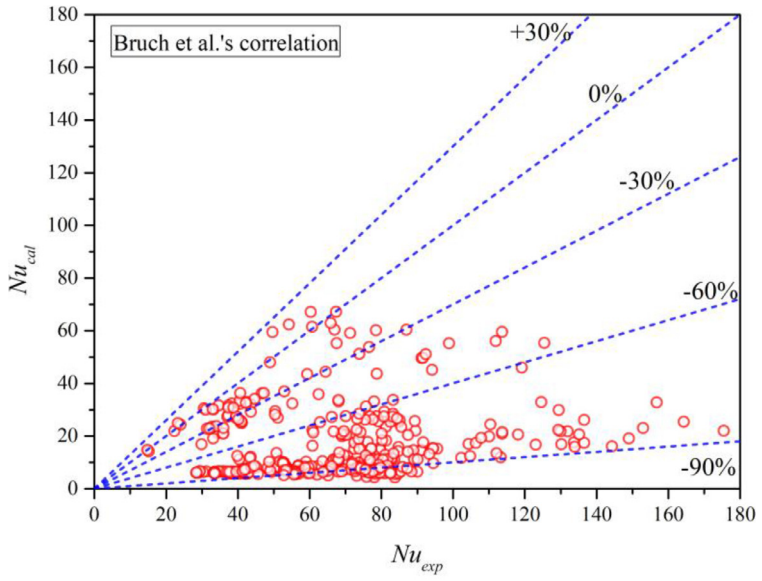

(a)

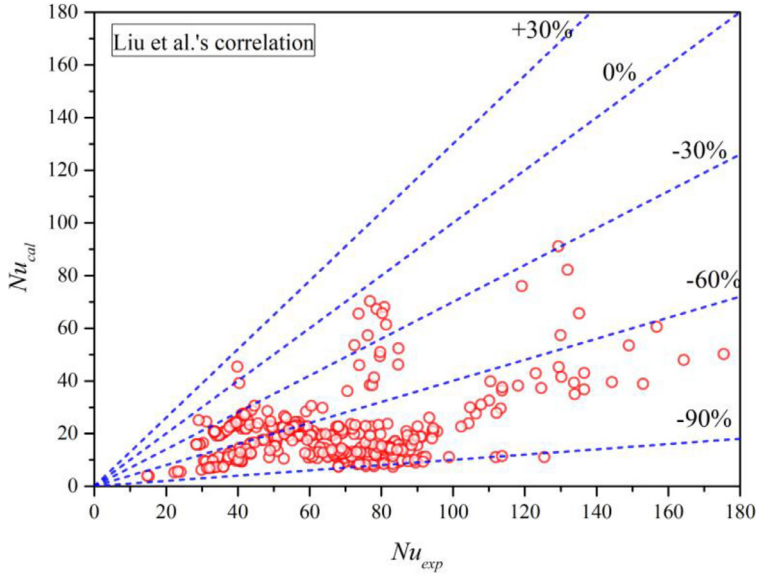

(b)

Fig. 13. Comparison of experimental Nusselt numbers and the calculated results based on the five published correlations.

Table 5
The five correlations used for comparison.

Authors	Correlation	Application condition
Bruch et al. [22]	$\frac{Nu_b}{Nu_{FC}} = \begin{cases} 1-75(Gr/\mathrm{Re}_b^{2.7})^{0.46}, \text{ for } Gr/\mathrm{Re}_b^{2.7} < 4.2\times10^{-5} \\ 13.5(Gr/\mathrm{Re}_b^{2.7})^{0.4}, \text{ for } Gr/\mathrm{Re}_b^{2.7} > 4.2\times10^{-5} \end{cases}$ where $Nu_{FC} = 0.0183\mathrm{Re}_b^{0.82}\overline{Pr}_b^{0.5}(\rho_w/\rho_b)^{0.3}$	Supercritical CO_2 in-tube flow P: 7.4–12 MPa; G: 50–590 kg•(m^2•s)$^{-1}$; T_{in}: 15–70 °C; Re:3600–1.8 × 10^6
Liu et al. [57]	$Nu = 0.01\mathrm{Re}_w^{0.9}\mathrm{Pr}_w^{0.5}(\frac{\rho_w}{\rho_b})^{0.906}(\frac{c_{p,w}}{c_{p,b}})^{-0.585}$	Supercritical CO_2 in-tube flow P: 7.5–8.5 MPa; G: 74.1–795.8 kg•(m^2•s)$^{-1}$; T_{in}: 25–67 °C
Forooghi and Hooman [40]	$Nu = 0.187\mathrm{Re}^{0.71}\mathrm{Pr}^{0.35}(\frac{\overline{c}_p}{c_{p,b}})^{0.5}(\frac{\rho_w}{\rho_b})^{0.3}$	Supercritical fluid in brazed plate heat exchanger Re: 800–4200; Pr: 3.2–4.2; Chevron angle: 60°
Lee et al. [55]	$Nu_{ref} = 2.205\times10^{-7}\mathrm{Re}_{ref}^{2.617}\mathrm{Pr}_{ref}^{0.4}$ $Nu_{ref} = 4.062\times10^{-10}\mathrm{Re}_{ref}^{3.029}\mathrm{Pr}_{ref}^{0.4}$ $Nu_{ref} = 1.416\times10^{-27}\mathrm{Re}_{ref}^{7.317}\mathrm{Pr}_{ref}^{0.4}$	Supercritical fluid in brazed plate heat exchanger Re: 2850–14,300;
Khan et al. [38]	$Nu = 0.1449\mathrm{Re}^{0.8414}\mathrm{Pr}^{0.35}(\frac{\mu}{\mu_w})^{0.14}$	Single phase fluid in brazed plate heat exchanger Re: 500–2500; Pr: 3.5–6.5; Chevron angle: 60°

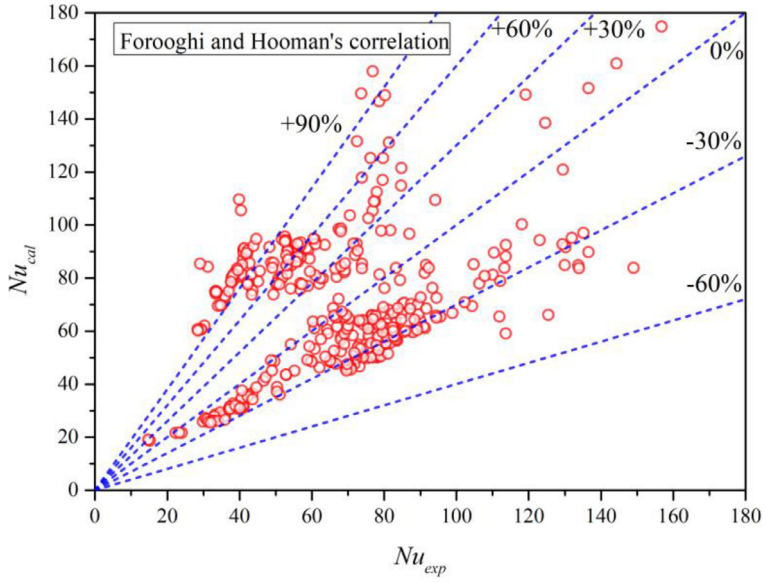

(c)

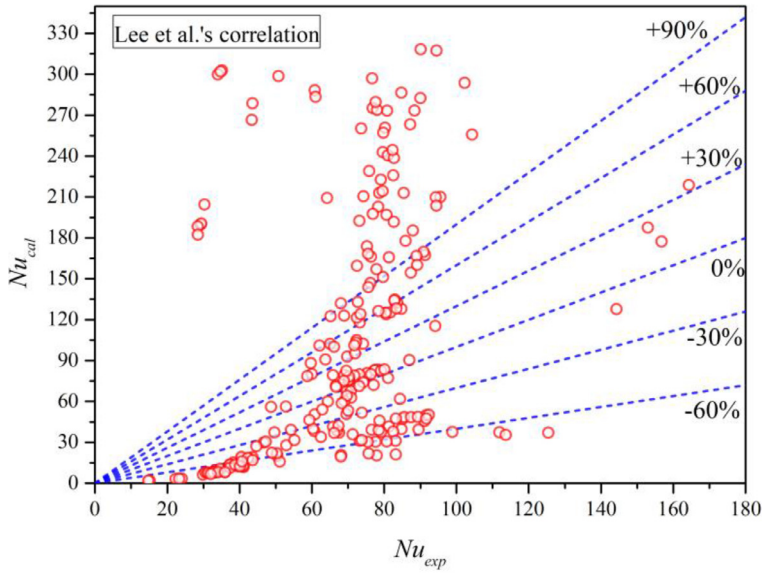

(d)

Fig. 13. Continued

Through analyzing the experimental data, it is found that the configuration (one-pass or two-pass) of the brazed plate heat exchangers has a great influence on the heat transfer performance. When the configuration is one-pass, the correlation is expressed as:

$$Nu = 0.33\mathrm{Re}_m^{0.804}\overline{Pr}_m^{0.1}\left(\frac{\rho_w}{\rho_m}\right)^{-0.1}\left(\frac{\bar{c}_p}{c_{p,m}}\right)^{0.093}\left(\frac{Gr}{\mathrm{Re}_m^{2.7}}\right)^{0.1} \quad (25)$$

When the configuration is two-pass, the correlation is expressed as:

$$Nu = 0.23\mathrm{Re}_m^{0.904}\overline{Pr}_m^{0.1}\left(\frac{\rho_w}{\rho_m}\right)^{-0.3}\left(\frac{\bar{c}_p}{c_{p,m}}\right)^{0.303}\left(\frac{Gr}{\mathrm{Re}_m^{2.7}}\right)^{0.222} \quad (26)$$

where $\bar{c}_p$ is the average specific heat and $\overline{Pr}_m$ is the Prandtl number calculated with $\bar{c}_p$:

$$\bar{c}_p = \frac{i_w - i_m}{T_w - T_m} \quad (27)$$

$$\overline{Pr}_m = \frac{\bar{c}_p \mu_m}{k_m} \quad (28)$$

The application ranges of the proposed correlations are: for the one-pass configuration, mass flux of 10.8 - 101.8 kg•(m^2•s)$^{-1}$, Reynolds number of 377.0 - 7754.3, Prandtl number of 1.2 - 14.2, CO_2 mean temperature of 21.3 - 79.9 °C, and pressure of 7.9 - 10.1 MPa; for the two-pass configuration, mass flux of 32.5 - 137.7 kg•(m^2•s)$^{-1}$, Reynolds number of 2230.0 - 6575.8, Prandtl number of 1.3 - 5.5, CO_2 mean temperature of 21.5 - 72.4 °C, and pressure of 7.9 - 10.1 MPa. In terms of the flow regime, as Blomerius

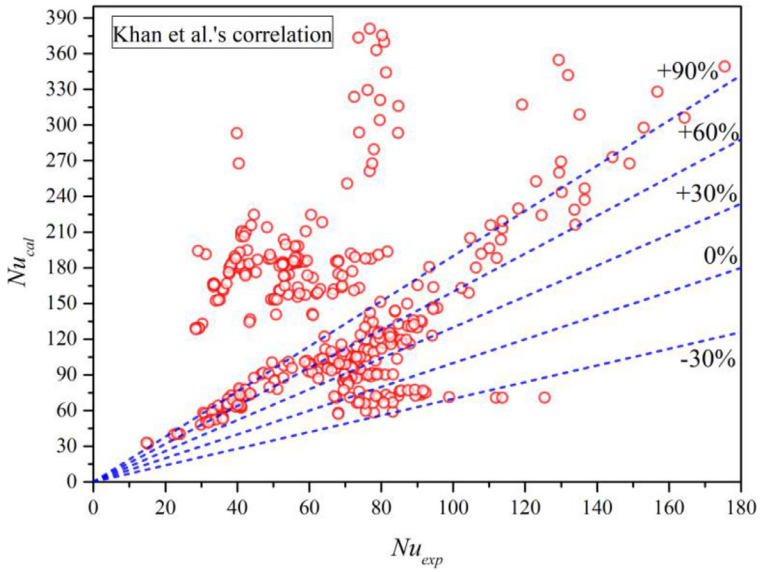

(e)

Fig. 13. Continued

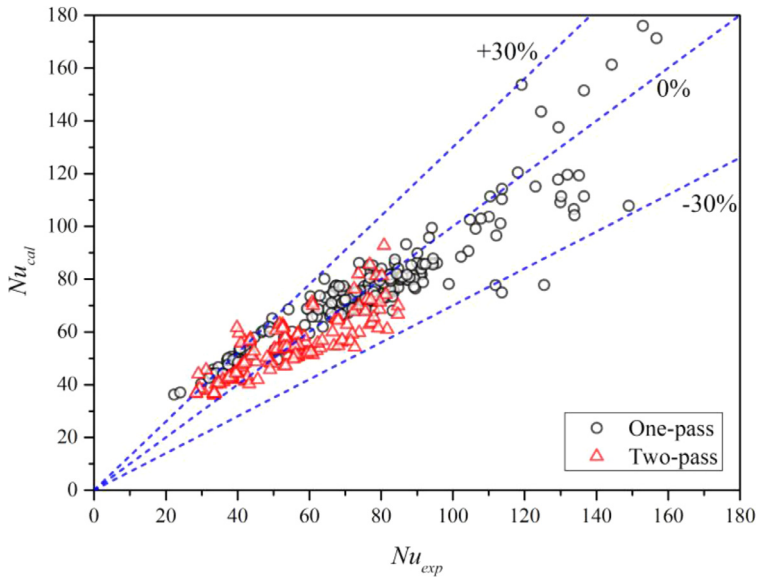

Fig. 14. Comparison of experimental data and the calculated results based on the proposed correlations.

et al. [64] indicated, the fluid flow in chevron-type plate heat exchangers is turbulent, even at low Reynolds numbers, due to the complex geometry. Moreover, through numerical research, Lee and Lee [65] found that with different chevron geometry, when the Reynolds number was less than 170–330, the Strouhal number was 0, which means that the flow was steady-state and laminar. Therefore, the flow in our research could be considered as turbulent. To clarify the influence of buoyancy force on the heat transfer, the correlations not considering $Gr/Re^{2.7}$ were established for comparison. The result shows that when $Gr/Re^{2.7}$ was considered, the coefficients of determination (R^2) of one-pass and two-pass correlations were respectively 0.78 and 0.70; while when $Gr/Re^{2.7}$ was not included, the R^2 consequently decreased to 0.69 and 0.64. Therefore, the consideration of $Gr/Re^{2.7}$ in these correlations could improve the accuracy, and thus the buoyancy force had an influence on the heat transfer.

Fig. 14 shows the comparison between experimental data and the calculated results based on the proposed correlations. The fitting is well, and 91.4% and 93.7% of the data points fall into the relative error range of ±30% with the one-pass and two-pass correlations, respectively. Regarding the mean absolute relative error, the value is 11.61% for one-pass and 12.82% for two-pass, which is much better than the correlations in Table 5.

4.3. Pressure drop

Fig. 15 gives the frictional pressure drop as the function of the CO_2 mean temperature under the condition of CO_2 inlet temperature of 97 °C, CO_2 mass flow rate of 0.0358 kg•s^{-1}, water inlet temperature of 13.1 °C and CO_2 inlet pressure of 9.4 MPa and 10 MPa. The pressure drop increases as the CO_2 mean temperature increases due to the decrease of the average density which leads

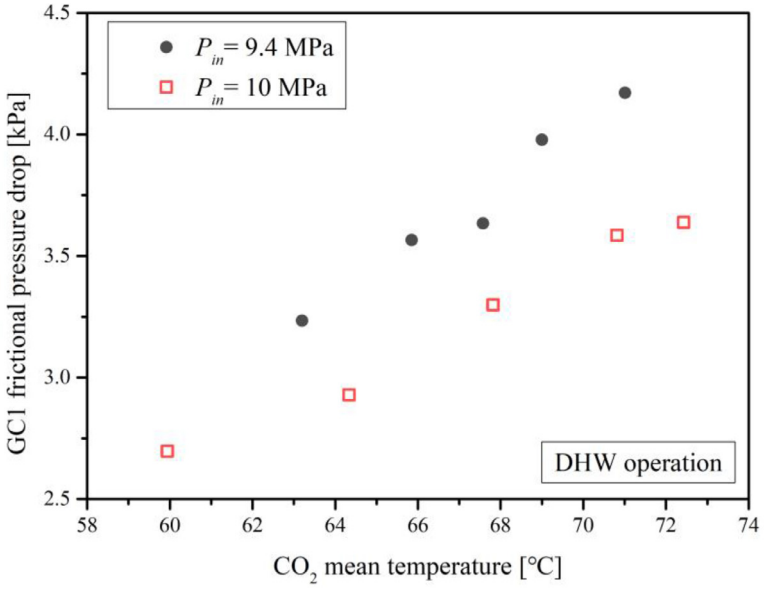

(a)

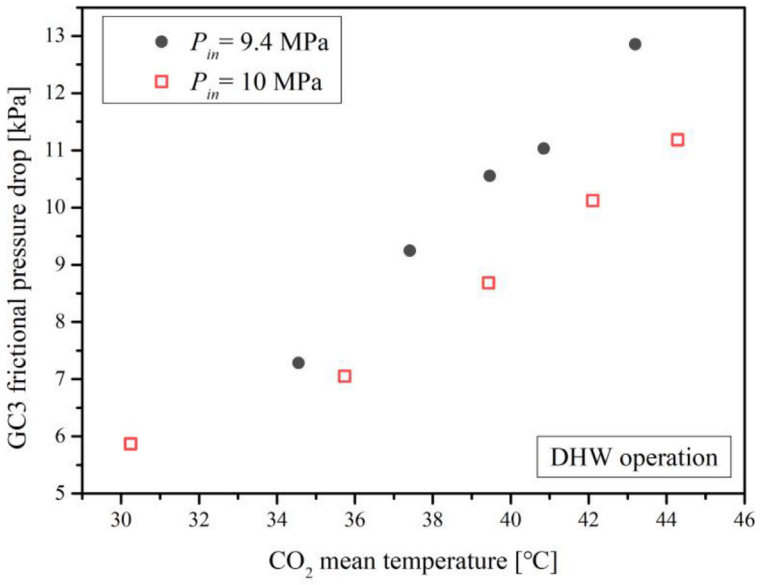

(b)

Fig. 15. Frictional pressure drop versus CO_2 mean temperature under different pressures.

to an increase in the refrigerant velocity. It can be seen that as the pressure increases, the pressure drop decreases. The increase of CO_2 pressure can result in a higher density and thus a lower velocity, which makes the pressure drop decreases. By comparing the values in Fig. 15(a) and (b), it can be discovered that the pressure drop of GC3 is higher than that of GC1. It is because the plate number of GC3 is less and hence the flow area is smaller. Despite the larger density caused by the lower temperature in GC3, the CO_2 flow velocity is higher, which leads to the increase of pressure drop.

Fig. 16 shows the variation of CO_2 frictional pressure drop with CO_2 mass flow rate. The results are obtained at CO_2 inlet pressure of 8.5 MPa, CO_2 inlet temperature of 80 °C, DHW inlet temperature of 12.6 °C, SH water inlet temperature of 30 °C, DHW mass flow rate of 0.0217 kg•s $^{-1}$ and SH water mass flow rate of 0.4133 kg•s $^{-1}$. It is demonstrated that the pressure drop increases from 3.29 kPa to 5.90 kPa for the GC1 and from 4.44 kPa to 9.19 kPa for the GC3 while the CO_2 mass flow rate increases from 0.0316 kg•s $^{-1}$ to 0.0433 kg•s $^{-1}$. As expected, the CO_2 mass flow rate has a significant influence on the frictional pressure drop, the higher mass flow rate can lead to the increase of pressure drop. Besides, it can also be observed that the slope of pressure drop in the GC3 is sharper than that in the GC1, and the difference of pressure drops between the GC3 and GC1 is larger at a higher CO_2 mass flow rate.

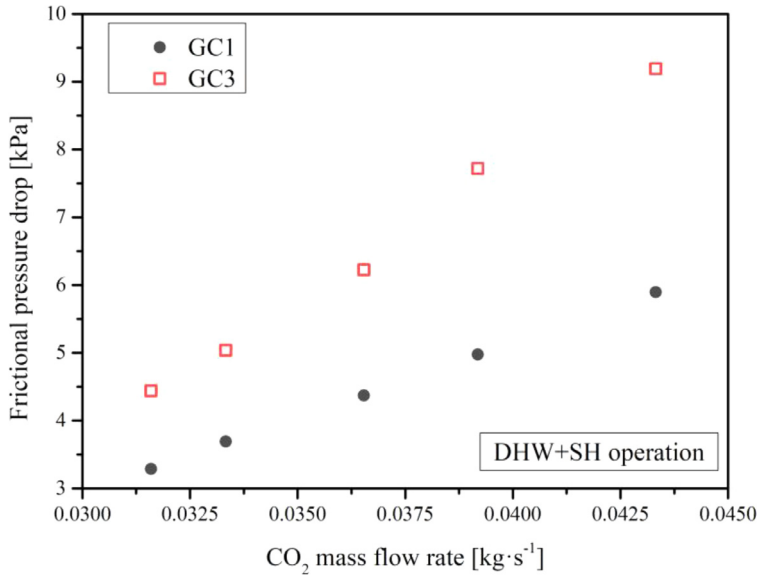

Fig. 16. Frictional pressure drop versus CO_2 mass flow rate.

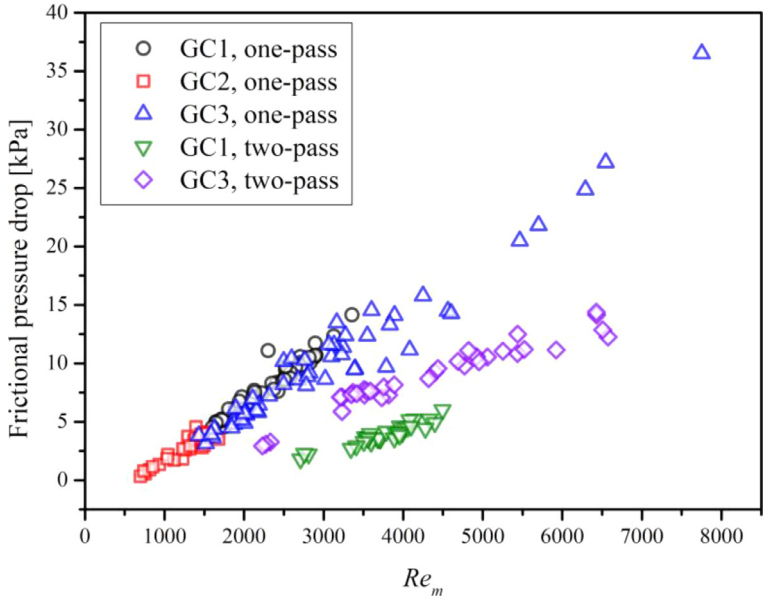

Fig. 17. Frictional pressure drop versus Reynolds number at CO_2 mean temperature.

Fig. 17 depicts all the data points of frictional pressure drop versus the Reynolds number at CO_2 mean temperature. Basically, the pressure drop increases with the increase of Reynolds number, regardless of the heat exchanger locations and the internal configurations. The GC2 shows the lowest pressure drop due to its maximal plate number and largest flow area. For the two-pass configuration, the pressure drop in the GC3 is obviously higher than that in the GC1; while for the one-pass configuration, the pressure drops in the GC1 and GC3 are at a roughly equal level with the same Reynolds number. It means that in the one-pass configuration, the effect of the changed plate number is neutralized by the variation of the density, and consequently the pressure drop scarcely changes. By contrast, the influence of the plate number dominates the magnitude of the pressure drop in the two-pass configuration, and hence the pressure drop of GC3 is higher than that of GC1. In general, the frictional pressure drop in the brazed plate heat exchangers is low, and the maximum frictional pressure drop is 36.49 kPa among all the values.

5. Conclusions

In this research, the heat transfer performance and pressure drop of three brazed plate heat exchangers serving as the gas coolers in a CO_2 system are investigated. The heat exchangers respectively function for the DHW reheating, SH heating and DHW preheating. The effects of the CO_2 inlet pressure, CO_2 inlet temperature, water inlet temperature, water mass flow rate and buoyancy force are analyzed. The experimental Nusselt numbers are compared with the calculated results based on the published correlations, and new heat transfer correlations are proposed to achieve higher prediction accuracy. Several conclusions can be drawn as follows.

(1) In the studied brazed plate heat exchangers, the averaged total, water side and CO_2 side heat transfer coefficients of all data points are respectively 1380.2, 6094.1 and 2035.0 $W•(m^2•K)^{-1}$, and the thermal resistance at the CO_2 side ba-

sically dominates the total heat transfer. The increase of CO_2 inlet pressure can reduce the heat transfer coefficients except at the high temperature region, i.e., the GC1 in this paper, and this reduction can reach up to 39.7% for CO_2 side heat transfer coefficient. The improvement of heat transfer coefficient by increasing the CO_2 mass flow rate is much more significant in the GC2 and GC3, and is lowest in the GC1.

(2) The influence of DHW inlet temperature on the heat transfer coefficients is not significant in the GC1 and GC2, but is more obvious in the GC3 that is directly linked to the water inlet. Under the DHW operation mode, the increase of water mass flow rate can enhance the heat transfer coefficient. However, under the SH operation mode, the increase of water mass flow rate conduces to the decreasing trend of heat transfer coefficients.

(3) The effect of CO_2 pressure on the buoyancy force depends on the temperature. The buoyancy force declines with the lower pressure when the CO_2 temperature is high in the GC1; while the buoyancy force is slightly improved by the decrease of pressure when the temperature is relatively low in the GC3. The lower CO_2 mass flow rate results in the higher buoyancy force. Moreover, except the GC3 at 8 MPa under the DHW+SH operation mode, the Nusselt number generally shows an increasing trend with the increase of buoyancy force.

(4) The heat transfer correlations of supercritical CO_2 in-tube flow are unusable because the complex geometry of the brazed plate heat exchange. The correlation for supercritical fluid in plate heat exchanger from Forooghi and Hooman shows the best prediction accuracy but is still not satisfactory with the mean absolute relative error of 41.1%. Thus, new correlations with higher accuracy are established considering the effects of thermodynamics properties and buoyancy force. The mean absolute relative errors of new correlations are respectively 11.61% and 12.82% for the one-pass and two-pass configurations.

(5) The frictional pressure drop in the studied brazed plate heat exchangers is low, and the maximum value is 36.51 kPa. Regardless of the location and the internal configuration of the heat exchangers, the pressure drop basically increases as the Reynolds number increases. The magnitude of the pressure drops in the GC1 and the GC3 with the one-pass and two-pass configurations had different behaviors, and the reduction of plate number had a higher influence in the two-pass configuration.

Declaration of Competing Interest

There is no conflict of interest.

CRediT authorship contribution statement

Alireza Zendehboudi: Conceptualization, Methodology, Formal analysis, Software, Investigation, Writing – original draft, Writing – review & editing. **Zuliang Ye:** Formal analysis, Software, Writing – original draft, Writing – review & editing. **Armin Hafner:** Supervision, Project administration, Funding acquisition. **Trond Andresen:** Writing – review & editing. **Geir Skaugen:** Writing – review & editing.

Acknowledgement

This research is supported by the European Union's Horizon 2020 research and innovation program, 'TRI-HP project' (grant number 814888). The author Ye is grateful for the financial support from the China Scholarship Council and the Department of Energy and Process Engineering, Norwegian University of Science and Technology for his overseas study at NTNU.

References

[1] C. Breidenich, D. Magraw, A. Rowley, J.W. Rubin, The kyoto protocol to the United Nations framework convention on climate change, Am. J. Int. Law 92 (2) (1998) 315–331.
[2] G. Lorentzen, The use of natural refrigerants: a complete solution to the CFC/HCFC predicament, Int. J. Refrig. 18 (3) (1995) 190–197.
[3] S.B. Riffat, C.F. Afonso, A.C. Oliveira, D.A. Reay, Natural refrigerants for refrigeration and air-conditioning systems, Appl. Therm. Eng. 17 (1) (1997) 33–42.
[4] C. Dang, E. Hihara, In-tube cooling heat transfer of supercritical carbon dioxide. Part 1. Experimental measurement, Int. J. Refrig. 27 (7) (2004) 736–747.
[5] M.M. Ehsan, Z. Guan, A.Y. Klimenko, A comprehensive review on heat transfer and pressure drop characteristics and correlations with supercritical CO_2 under heating and cooling applications, Renew. Sustain. Energy Rev. 92 (2018) 658–675.
[6] G. Lorentzen, J. Pettersen, A new, efficient and environmentally benign system for car air-conditioning, Int. J. Refrig. 16 (1) (1993) 4–12.
[7] B.T. Austin, K. Sumathy, Transcritical carbon dioxide heat pump systems: a review, Renew. Sustain. Energy Rev. 15 (8) (2011) 4013–4029.
[8] M. Saikawa, K. Hashimoto, T. Kobayakawa, K. Kusakari, M. Ito, H. Sakakibara, Development of prototype of CO_2 heat pump water heater for residential use, in: IIR-Gustav Lorentzen conference on natural working fluids at Purdue (4; West Lafayette IN 2000-07-25) /Conférence IIR-Gustav Lorentzen sur les fluides actifs naturels à Purdue (4; West Lafayette IN 2000-07-25), Paris, Institut international du froid, 2000, pp. 97–102.
[9] F. Zhang, Y. Zhu, C. Li, P. Jiang, Thermodynamic optimization of heat transfer process in thermal systems using CO_2 as the working fluid based on temperature glide matching, Energy 151 (2018) 376–386.
[10] M. Saikawa, S. Koyama, Thermodynamic analysis of vapor compression heat pump cycle for tap water heating and development of CO_2 heat pump water heater for residential use, Appl. Therm. Eng. 106 (2016) 1236–1243.
[11] K. Nawaz, B. Shen, A. Elatar, V. Baxter, O. Abdelaziz, Performance optimization of CO_2 heat pump water heater, Int. J. Refrig. 85 (2018) 213–228.
[12] C. Arpagaus, F. Bless, J. Schiffmann, S.S. Bertsch, Multi-temperature heat pumps: a literature review, Int. J. Refrig. 69 (2016) 437–465.
[13] P. Nekså, CO_2 heat pump systems, Int. J. Refrig. 25 (4) (2002) 421–427.
[14] J. Stene, Residential CO_2 heat pump system for combined space heating and hot water heating, Int. J. Refrig. 28 (8) (2005) 1259–1265.
[15] J. Stene, Integrated CO_2 Heat Pump Systems for Space Heating and Hot Water Heating in Low-Energy Houses and Passive Houses, 32, International Energy Agency (IEA) Heat Pump Programme–Annex, 2007.
[16] J. Stene, M.J. Alonso, Field Measurements–Heat Pump Systems in NZEB, SINTEF Academic Press, 2016.
[17] R.L. Amalfi, J.R. Thome, V. Solotych, J. Kim, High resolution local heat transfer and pressure drop infrared measurements of two-phase flow of R245fa within a compact plate heat exchanger, Int. J. Heat Mass Transf. 103 (2016) 791–806.
[18] R. Barzegarian, M.K. Moraveji, A. Aloueyan, Experimental investigation on heat transfer characteristics and pressure drop of BPHE (brazed plate heat exchanger) using TiO 2 –water nanofluid, Exp. Therm. Fluid Sci. 74 (2016) 11–18.
[19] J. Xie, D. Liu, H. Yan, G. Xie, S.K.S. Boetcher, A review of heat transfer deterioration of supercritical carbon dioxide flowing in vertical tubes: heat transfer behaviors, identification methods, critical heat fluxes, and heat transfer correlations, Int. J. Heat Mass Transf. 149 (2020) 119233.
[20] L. Cheng, G. Ribatski, J.R. Thome, Analysis of supercritical CO_2 cooling in macro- and micro-channels, Int. J. Refrig. 31 (8) (2008) 1301–1316.
[21] S.M. Liao, T.S. Zhao, An experimental investigation of convection heat transfer to supercritical carbon dioxide in miniature tubes, Int. J. Heat Mass Transf. 45 (2002) 5025–5034.
[22] A. Bruch, A. Bontemps, S. Colasson, Experimental investigation of heat transfer of supercritical carbon dioxide flowing in a cooled vertical tube, Int. J. Heat Mass Transf. 52 (11–12) (2009) 2589–2598.
[23] Y.-Y. Bae, H.-Y. Kim, D.-J. Kang, Forced and mixed convection heat transfer to supercritical CO_2 vertically flowing in a uniformly-heated circular tube, Exp. Therm. Fluid Sci. 34 (8) (2010) 1295–1308.
[24] S. Liu, Y. Huang, G. Liu, J. Wang, L.K.H. Leung, Improvement of buoyancy and acceleration parameters for forced and mixed convective heat transfer to supercritical fluids flowing in vertical tubes, Int. J. Heat Mass Transf. 106 (2017) 1144–1156.
[25] D.E. Kim, M.H. Kim, Experimental study of the effects of flow acceleration and buoyancy on heat transfer in a supercritical fluid flow in a circular tube, Nucl. Eng. Des. 240 (10) (2010) 3336–3349.
[26] S. Zhang, X. Xu, C. Liu, X. Liu, Z. Ru, C. Dang, Experimental and numerical comparison of the heat transfer behaviors and buoyancy effects of supercritical CO_2 in various heating tubes, Int. J. Heat Mass Transf. 149 (2020) 119074.
[27] R.-N. Xu, F. Luo, P.-X. Jiang, Buoyancy effects on turbulent heat transfer of supercritical CO_2 in a vertical mini-tube based on continuous wall temperature measurements, Int. J. Heat Mass Transf. 110 (2017) 576–586.
[28] P. Forooghi, K. Hooman, Numerical study of turbulent convection in inclined pipes with significant buoyancy influence, Int. J. Heat Mass Transf. 61 (2013) 310–322.

[29] J.H. Bae, J.Y. Yoo, D.M. McEligot, Direct numerical simulation of heated CO_2 flows at supercritical pressure in a vertical annulus at Re=8900, Phys. Fluids 20 (5) (2008) 055108.
[30] P. Forooghi, I.A. Abdi, M. Dahari, K. Hooman, Buoyancy induced heat transfer deterioration in vertical concentric and eccentric annuli, Int. J. Heat Mass Transf. 81 (2015) 222–233.
[31] S.H. Lee, Numerical study of convective heat transfer to supercritical water in rectangular ducts, Int. Commun. Heat Mass Transfer 37 (10) (2010) 1465–1470.
[32] I. Gherasim, M. Taws, N. Galanis, C.T. Nguyen, Numerical and experimental investigation of buoyancy effects in a plate heat exchanger, Appl. Therm. Eng. 51 (1–2) (2013) 347–363.
[33] P. Forooghi, K. Hooman, Effect of buoyancy on turbulent convection heat transfer in corrugated channels – a numerical study, Int. J. Heat Mass Transf. 64 (2013) 850–862.
[34] Y. Zhu, Y. Huang, S. Lin, C. Li, P. Jiang, Study of convection heat transfer of CO_2 at supercritical pressures during cooling in fluted tube-in-tube heat exchangers, Int. J. Refrig. 104 (2019) 161–170.
[35] W.W. Focke, J. Zachariades, I. Olivier, The effect of the corrugation inclination angle on the thermohydraulic performance of plate heat-exchangers, Int. J. Heat Mass Transf. 28 (8) (1985) 1469–1479.
[36] H. Martin, A theoretical approach to predict the performance of chevron-type plate heat exchangers, Chem. Eng. Process. 35 (4) (1996) 301–310.
[37] G.A. Longo, Refrigerant R134a condensation heat transfer and pressure drop inside a small brazed plate heat exchanger, Int. J. Refrig. 31 (5) (2008) 780–789.
[38] T.S. Khan, M.S. Khan, M.-.C. Chyu, Z.H. Ayub, Experimental investigation of single phase convective heat transfer coefficient in a corrugated plate heat exchanger for multiple plate configurations, Appl. Therm. Eng. 30 (8–9) (2010) 1058–1065.
[39] J. Huang, T.J. Sheer, M. Bailey-McEwan, Heat transfer and pressure drop in plate heat exchanger refrigerant evaporators, Int. J. Refrig. 35 (2) (2012) 325–335.
[40] P. Forooghi, K. Hooman, Experimental analysis of heat transfer of supercritical fluids in plate heat exchangers, Int. J. Heat Mass Transf. 74 (2014) 448–459.
[41] D. Huang, Z. Wu, B. Sunden, Pressure drop and convective heat transfer of Al_2O_3/water and MWCNT/water nanofluids in a chevron plate heat exchanger, Int. J. Heat Mass Transf. 89 (2015) 620–626.
[42] G.A. Longo, S. Mancin, G. Righetti, C. Zilio, A new model for refrigerant boiling inside Brazed Plate Heat Exchangers (BPHEs), Int. J. Heat Mass Transf. 91 (2015) 144–149.
[43] K. Nilpueng, S. Wongwises, Experimental study of single-phase heat transfer and pressure drop inside a plate heat exchanger with a rough surface, Exp. Therm. Fluid Sci. 68 (2015) 268–275.
[44] K. Sarraf, S. Launay, L. Tadrist, Complex 3D-flow analysis and corrugation angle effect in plate heat exchangers, Int. J. Therm. Sci. 94 (2015) 126–138.
[45] R.L. Amalfi, J.R. Thome, High resolution infrared measurements of single-phase flow of R245fa and R236fa within a compact plate heat exchanger, Part 1: experimental setup and pressure drop results, Appl. Therm. Eng. 101 (2016) 545–554.
[46] R.L. Amalfi, J.R. Thome, High resolution infrared measurements of single-phase flow of R245fa and R236fa within a compact plate heat exchanger, Part 2: heat transfer results, Appl. Therm. Eng. 101 (2016) 555–563.
[47] G.A. Longo, S. Mancin, G. Righetti, C. Zilio, HFO1234ze(E) vaporisation inside a Brazed Plate Heat Exchanger (BPHE): comparison with HFC134a and HFO1234yf, Int. J. Refrig. 67 (2016) 125–133.
[48] A. Desideri, J. Zhang, M.R. Kærn, T.S. Ommen, J. Wronski, V. Lemort, F. Haglind, An experimental analysis of flow boiling and pressure drop in a brazed plate heat exchanger for organic Rankine cycle power systems, Int. J. Heat Mass Transf. 113 (2017) 6–21.
[49] M. Imran, M. Usman, Y. Yang, B.-.S. Park, Flow boiling of R245fa in the brazed plate heat exchanger: thermal and hydraulic performance assessment, Int. J. Heat Mass Transf. 110 (2017) 657–670.
[50] K. Nilpueng, T. Keawkamrop, H.S. Ahn, S. Wongwises, Effect of chevron angle and surface roughness on thermal performance of single-phase water flow inside a plate heat exchanger, Int. Commun. Heat Mass Transfer 91 (2018) 201–209.
[51] S.H. Pourhoseini, N. Naghizadeh, H. Hoseinzadeh, Effect of silver-water nanofluid on heat transfer performance of a plate heat exchanger: an experimental and theoretical study, Powder Technol. 332 (2018) 279–286.
[52] B.H. Shon, C.W. Jung, O.J. Kwon, C.K. Choi, Y.Tae Kang, Characteristics on condensation heat transfer and pressure drop for a low GWP refrigerant in brazed plate heat exchanger, Int. J. Heat Mass Transf. 122 (2018) 1272–1282.
[53] K. Miyata, H. Mori, T. Taniguchi, S. Umezawa, K. Sugita, Effect of the chevron angle on cooling heat transfer characteristics of supercritical pressure fluids in plate heat exchangers, Heat Transfer Eng. 40 (12) (2018) 1007–1022.
[54] G.A. Longo, S. Mancin, G. Righetti, C. Zilio, Boiling of the new low-GWP refrigerants R1234ze(Z) and R1233zd(E) inside a small commercial brazed plate heat exchanger, Int. J. Refrig. 104 (2019) 376–385.
[55] C. Lee, J.-.W. Ko, H.Y. Ji, S.-.C. Kim, Experimental assessment of convective heat transfer and pressure drop correlation of R1234ze(E) for a supercritical heat exchanger in the organic Rankine cycle, J. Mech. Sci. Technol. 34 (11) (2020) 4809–4818.
[56] I. Fazeli, M.R. Sarmasti Emami, A. Rashidi, Investigation and optimization of the behavior of heat transfer and flow of MWCNT-CuO hybrid nanofluid in a brazed plate heat exchanger using response surface methodology, Int. Commun. Heat Mass Transfer 122 (2021) 105175.
[57] Z.-.B. Liu, Y.-.L. He, Y.-.F. Yang, J.-.Y. Fei, Experimental study on heat transfer and pressure drop of supercritical CO_2 cooled in a large tube, Appl. Therm. Eng. 70 (1) (2014) 307–315.
[58] R.J. Moffat, Describing the uncertainties in experimental results, Exp. Therm. Fluid Sci. 1 (1) (1988) 3–17.
[59] I.L. Pioro, R.B. Duffey, Heat Transfer and Hydraulic Resistance at Supercritical Pressures in Power Engineering Applications, ASME Press, 2007.
[60] T. Ma, W.-x. Chu, X.-y. Xu, Y.-t. Chen, Q.-w. Wang, An experimental study on heat transfer between supercritical carbon dioxide and water near the pseudo–critical temperature in a double pipe heat exchanger, Int. J. Heat Mass Transf. 93 (2016) 379–387.
[61] J.D. Jackson, W.B. Hall, in: Influence of Buoyancy on Heat Transfer to Fluids Flowing in Vertical Tubes Under Turbulent conditions, 2, Institution of Mechanical Engineers, Conference Publications, 1979, pp. 613–640.
[62] Q. Zhang, H. Li, X. Kong, J. Liu, X. Lei, Special heat transfer characteristics of supercritical CO_2 flowing in a vertically-upward tube with low mass flux, Int. J. Heat Mass Transf. 122 (2018) 469–482.
[63] G.-.W. Zhang, P. Hu, L.-.X. Chen, M.-.H. Liu, Experimental and simulation investigation on heat transfer characteristics of in-tube supercritical CO_2 cooling flow, Appl. Therm. Eng. 143 (2018) 1101–1113.
[64] H. Blomerius, C. Holsken, N.K. Mitra, Numerical investigation of flow field and heat transfer in cross-corrugated ducts, J Heat Trans-T Asme 121 (2) (1999) 314–321.
[65] J. Lee, K.-.S. Lee, Flow characteristics and thermal performance in chevron type plate heat exchangers, Int. J. Heat Mass Transf. 78 (2014) 699–706.